https://doi.org/10.5194/egusphere-2026-1741
Preprint. Discussion started: 1 June 2026

First demonstration of the combination of observations and datasets from diverse instruments (in a coordinated experiment using KAIRA, EISCAT, GNSS) that enables the extraction of new information about the ionosphere

Biagio Forte[1], Andrzej Krankowski[2], Kacper Kotulak[2], Derek McKay[3], Ingemar Häggström[4], John S. Morgan[5], Richard A. Fallows[6], Mario M. Bisi[6], Paul Kinsler[1], Leszek Błaszkiewicz[2], Tianchu Lu[1], Antti Kero[7], Paweł Flisek[2], Adam Fron[2], Michal Kownacki[2], Bartosz Radzanowski[2], Katarzyna Beser[8]

[1]Department of Electronic and Electrical Engineering, University of Bath, BA2 7AY Bath, United Kingdom: b.forte@bath.ac.uk, pk741@bath.ac.uk, tl877@bath.ac.uk.

[2]Space Radio-Diagnostics Research Centre, University of Warmia and Mazury in Olsztyn, Poland, kand@uwm.edu.pl, kacper.kotulak@uwm.edu.pl, leszek.blaszkiewicz@uwm.edu.pl, srrc@uwm.edu.pl, adam.fron@uwm.edu.pl, michal.kownacki@student.uwm.edu.pl, bartosz.radzanowski@uwm.edu.pl.

[3]Aalto University Metsähovi Radio Observatory, Metsähovintie 114, FI-02540 Kylmälä, Finland, derek.mckay@aalto.fi.

[4] EISCAT Scientific Association, Kiruna, Sweden, ingemar.haggstrom@eiscat.se.

[5] CSIRO Space and Astronomy, Kensington, Australia; e-mail: John.Morgan@csiro.au.

[6]RAL Space, United Kingdom Research and Innovation (UKRI) – Science & Technology Facilities Council (STFC) – Rutherford Appleton Laboratory (RAL), Harwell Campus, United Kingdom: richard.fallows@stfc.ac.uk, mario.bisi@stfc.ac.uk.

[7]Sodankylä Geophysical Observatory, FIN-99600 Sodankylä, Finland: antti.kero@sgo.fi.

[8]New Jersey Institute of Technology, 323 Dr Martin Luther King Jr Blvd, Newark, NJ 07102, USA: katarzyna.beser@njit.edu.

Correspondence to: Biagio Forte (b.forte@bath.ac.uk)

https://doi.org/10.5194/egusphere-2026-1741
Preprint. Discussion started: 1 June 2026

Abstract. The plasma of the Earth's ionosphere introduces effects on radio waves that traverse it. Propagation effects reflect the presence of the bulk ionisation along the ray path as well as the presence of inhomogeneities (or irregularities) in the spatial distribution of the plasma (or electron) density. Ionospheric propagation effects are visible on radio signals received from artificial satellites (with radio wave frequencies approximately between the VHF and the C band), on terrestrial HF propagation, and on radio waves (between VHF and L/C bands) typically utilised in radio astronomy.

The presence of propagation effects can be utilised to deduce properties of the ionosphere: for example, through the dispersion of radio signals from satellite navigation satellites it is possible to appreciate the spatial and temporal evolution of the bulk of the ionisation in the ionosphere all over the Earth. On the other hand, properties of ionospheric irregularities (spatial and temporal gradients in the background ionisation) can be deduced from the presence of phase fluctuations and scintillation (whose magnitude decreases with frequency). However, the capability of detecting the presence of plasma structures depend upon the sensitivity of the instruments utilised.

Here, an experiment (the first of this kind) was conducted in the European auroral and polar sectors to demonstrate how the combination of diverse instruments and datasets enables the extraction of new information about the ionosphere and its spatio-temporal evolution, based on the combination of observations from a smaller radio telescope (KAIRA), incoherent scatter radars (EISCAT/ESR), satellite radio receivers (GNSS), and an ionosonde.

In particular, KAIRA (an instrument built using LOFAR radio telescope technology) was utilised to simultaneously collect all-sky images and beam-formed VHF scintillation on radio signals received from the source Cassiopeia A (Cas A). At the same time, the EISCAT incoherent scatter radar was utilised to measure profiles of electron density along lines of sight to Cas A closely matching those used in KAIRA observations. Finally, temporal fluctuations in the ionospheric Total Electron Content (rate of change of TEC, ROT) from Global Navigation Satellite Systems (GNSS) signals received at ground stations in the surrounding of KAIRA and EISCAT, were utilised to infer large-scale conditions in the ionosphere at the time of the observations as well as the type of ionisation gradients originating specific propagation effects.

The results of this experiment demonstrate for the first time that stronger ionisation gradients ($|\mathrm{ROT}| \gtrsim 0.2$ TECU min^{-1}) that are extended over a wider range of altitudes in the ionosphere can be detected through EISCAT electron density profiles as well as through propagation effects detectable through GNSS (phase fluctuations) and KAIRA (VHF scintillation). The experiment's results also indicate that weaker ionisation gradients ($|\mathrm{ROT}| \lesssim 0.2$ TECU min^{-1}) can induce VHF scintillation but may not be detectable through GNSS and EISCAT (their sensitivity and resolution is limited). The position and shape of astronomical sources appears to be affected by two concurring aspects: slower trends (due to changes in the ionisation with gradients probably having $|\mathrm{ROT}| \ll 0.2$ TECU min^{-1} as a consequence of horizontal plasma drift and/or local ionospheric mechanisms) and degradations in the estimates of source position and shape (due to scintillation, when noise and other parts of the sky around a given source have higher contributions – an effect similar to optical blurring).

https://doi.org/10.5194/egusphere-2026-1741
Preprint. Discussion started: 1 June 2026

By combining the evidence from diverse instruments and datasets through a novel methodology, the experiment demonstrates that ionisation gradients in the ionosphere can occur over multiple spatial scales (both horizontally and in altitude). Whilst observations from modern radio telescopes (e.g., LOFAR, MWA, SKA-Low) provide a new way to detect and characterise the spatial and temporal evolution of plasma gradients in the ionosphere (due to a higher sensitivity), it is their combination with observations from traditional ionospheric instruments like GNSS, rather than their use in isolation, that enables novel understanding of ionospheric physics through a more accurate reconstruction of the ionospheric state over multiple spatial scales in the presence of different space weather conditions. This study provides a methodology to extract new information on ionospheric structures across multiple spatial scales based on the combination of observations from radio telescopes, GNSS, and incoherent scatter radars, which can be applied to other current and future instruments.

https://doi.org/10.5194/egusphere-2026-1741
Preprint. Discussion started: 1 June 2026

1 Introduction

The Earth's ionosphere is a magnetised plasma (i.e., free ions and electrons in the presence of an independent geomagnetic field): its behaviour is determined by the combination of solar and geomagnetic conditions together with its interaction with the neutral part of the Earth's atmosphere (Kelley, 2009). The presence of the ionospheric plasma around the Earth introduces various effects in the propagation of radio waves (with radio wave frequencies between VHF and C band capable of traversing the ionosphere) that traverse it (Kelley, 2009).

Due to its dispersive nature, the ionospheric plasma introduces an advance in the phase (and a group delay) of radio waves propagating through, which is proportional to the electron density integrated along the ray path direction (or Total Electron Content, TEC). The additional presence of inhomogeneities (or irregularities) in the spatial distribution of the ionospheric electron density introduces distortions along the wavefront of radio waves traversing them: as inhomogeneities tend to drift, these distortions in the wavefronts manifest as temporal fluctuations in the phase and intensity of the received radio waves (Aarons, 1997).

Two types of propagation effects can be associated with ionospheric irregularities: (a) phase fluctuations originating from larger-scale ionospheric plasma structures, large enough to originate a spatial and temporal gradient in TEC (Aarons, 1997; Forte et al., 2024) and (b) scintillation in the phase and intensity of radio waves propagating through smaller-scale ionospheric plasma structures (Booker and MajidiAhi, 1981; Forte et al., 2017). In the latter case, a stochastic distribution of irregularities in the propagation medium that is drifting across the propagation direction induces a distortion along the wavefront: this distortion leads to constructive and destructive interference with distance which can be observed as temporal phase fluctuations and scintillation in the phase and intensity of the radio waves at the receiving point. Whilst phase fluctuations can be generated by irregularities with large-to-small spatial scales, intensity fluctuations (or amplitude scintillation) are produced by irregularities with small spatial scales (typical of the inertial subrange of spatial scales over which electron density inhomogeneities form).

Propagation effects (i.e., phase fluctuations and intensity scintillation) induced by ionospheric irregularities can be present on radio waves transmitted from artificial satellites orbiting around planet Earth and observed by means of ground radio receivers (Aarons, 1997; Forte et al., 2017; John et al., 2021a; John et al., 2021b; Forte et al., 2024) as well as on radio waves emitted from radio sources far from Earth and observed by means of radio telescopes (Hewish et al., 1964; Little and Hewish, 1966; Budden and Uscinski, 1970; Yamauchi et al., 1996; Bisoi et al., 2014; Fallows et al., 2014; Flisek et al., 2023; Morgan et al., 2018).

https://doi.org/10.5194/egusphere-2026-1741
Preprint. Discussion started: 1 June 2026

In the case of observations from radio telescopes, propagation effects such as scintillation from either the ionosphere and/or the interplanetary medium can be observed along the specific direction to a given radio source (i.e., beam-formed observations) (Fallows et al., 2014; McKay, 2018; McKay-Bukowski et al., 2015; Morgan et al. 2018; Morgan et al., 2019; Morgan et al., 2023; Waszewski et al., 2022). Ionospheric propagation effects also manifest on typical astronomical observations of the sky (e.g., interferometric imaging), such as the apparent movement of a source (due to gradients in the bulk of ionisation) and/or the blurring of a source (due to scintillation): shifts in the locations of astronomical sources measure ionospheric phase gradients on a spatial scale approximately of the diameter of the observing instrument (Hewish et al, 1964; Little and Hewish, 1966; Loi et al. 2015; McKay, 2018).

A detailed understanding of such propagation effects will be crucial for optimising future radio astronomical observations like those from the Square Kilometre Array Observatory (SKAO) as well as to extract information on the ionosphere in a reliable approach. This is also true for proposed systems on the far side of the Moon (Gorgolewski, 1965), notwithstanding the fact that the plasma frequency limit (the lowest radio wave frequency that can propagate through a plasma) is significantly lower in the heliosphere than it is in the ionosphere (where it is approximately of the order of few MHz).

However, this quest for understanding also provides an opportunity: propagation effects can be used to retrieve information about the plasma propagation medium such as its distribution of drift velocities, of electron density, and of electron density gradients (i.e., information about how irregularities form and evolve in the plasma). Thus, this introduces the possibility to use radio telescopes as instruments to monitor the state of the ionosphere as well as of the heliosphere during different space weather conditions. However, this possibility does depend on an accurate description of both the plasma behaviour and its effects on radio propagation.

For example, low intensity scintillation can be approximated by assuming a weak scattering approximation based on a single phase-changing screen along which irregularities are assumed to be distributed according to a typically turbulent spatial spectrum: in this case, intensity scintillation can be utilised to infer location and drift velocity of the irregularities (Ishimaru, 1978). On the other hand, higher scintillation originates from multiple scattering, a situation which requires an understanding of the distribution of irregularities also along the propagation direction (Uscinski, 1977; Booker and Majidiahi, 1981).

This work describes a multi-instrument experiment investigating frequency-dependent ionospheric propagation effects occurring in the European auroral and polar sectors, including how these effects originate from ionospheric irregularities, and what their impact is during the observation of a radio source. The experiment was based on the combination of KAIRA (Kilpisjärvi Atmospheric Imaging Receiver Array) beam-formed observations of VHF scintillation on radio waves received from the Cas A radio source (Fallows et al., 2014; McKay-Bukowski et al., 2015; De Gasperin et al., 2020), KAIRA all-sky images (Kero et al;, 2014; McKay et al., 2015; Chaur et al., 2018; McKay, 2018), GNSS (Global Navigation Satellite Systems)

https://doi.org/10.5194/egusphere-2026-1741
Preprint. Discussion started: 1 June 2026

observations of L-band phase fluctuations, and electron density profiles observed through the EISCAT UHF Incoherent Scatter Radar (ISR) in Tromsø (Forte et al, 2013; Forte et al., 2017; John et al., 2021a; John et al., 2021b).

The objective of the analysis presented here is to understand, based on observations from different instruments, how ionospheric irregularities occurring within a common volume in the auroral ionosphere generate different types of frequency-dependent propagation effects and how these effects can be utilised to infer knowledge about the ionosphere.

More specifically, the questions that this study intends to address are as follows. (1) On the basis of the experimental evidence available from KAIRA beam-formed VHF scintillation, GNSS phase fluctuations, and EISCAT electron density observations, what information can be deduced about ionospheric irregularities and the propagation effects associated with them? (2) How can ionospheric propagation disturbances affecting all-sky images be utilised to deduce information about ionospheric structures and processes, amidst the evidence provided by other instruments?

Although this study is conducted in the auroral ionosphere, its general principles and methodology can be generalised to combine traditional ionospheric observations (such as through GNSS) and new ionospheric observations carried out with modern radio telescopes. The methodology outlined here can indeed be applied to any LOFAR imaging and LOFAR beam-formed VHF scintillation observations, to similar observations from other radio telescopes, and even to observations in the middle latitude ionosphere in the presence of ionospheric irregularities. Indeed, as the KAIRA instrument uses LOFAR-design hardware and software, the technique, method of data processing and even the observing scripts can be directly applied to any LOFAR station (McKay et al., 2015).

2 Data and Methodology

In order to demonstrate whether and how diverse observations and datasets can be combined to extract new information about the ionosphere, an experiment was devised and conducted in the European auroral and polar latitudes sector, where there can be more active ionospheric conditions (Fig. 1). The experiment is based on the comparison and combination of observations of ionospheric propagation effects occurring simultaneously in a common volume, detected through three different instruments: ground GNSS receivers (providing observations of temporal fluctuations in the slant TEC along the directions to each satellite in view, a measure of phase fluctuations), KAIRA (providing observations of radio wave scintillation on VHF radio wave frequencies received from Cas A as well as images of the source Cas A deduced from all-sky images), and EISCAT UHF/ESR Incoherent Scatter Radars (providing profiles of electron density along directions to Cas A as well as along magnetic field lines).

https://doi.org/10.5194/egusphere-2026-1741
Preprint. Discussion started: 1 June 2026

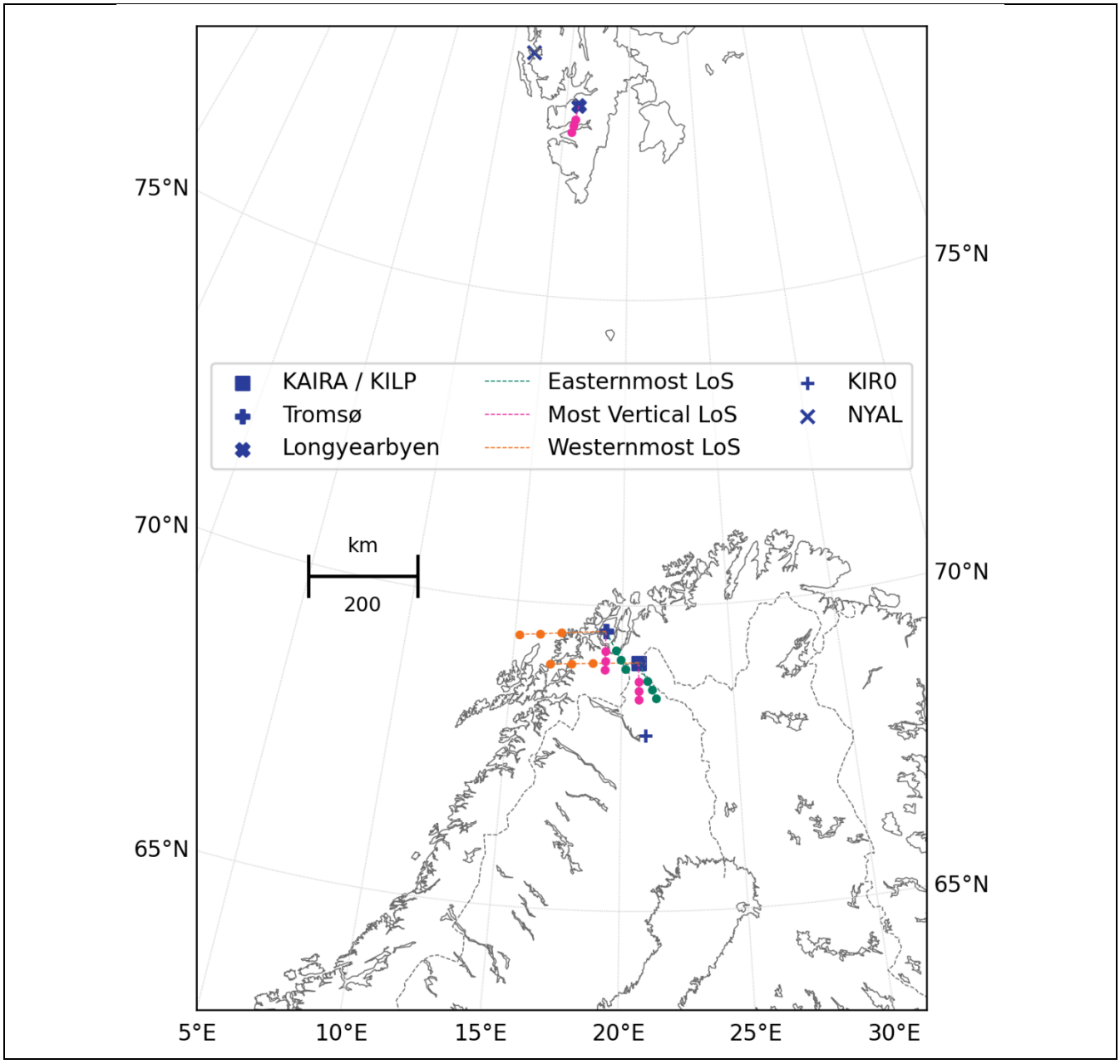

Figure 1: The geometry of the experiment, with lines of sights from radars and KAIRA beams intersecting different shell heights at 200 km, 300 km and 400 km (corresponding to different dots along easternmost, most vertical, and westernmost directions).

https://doi.org/10.5194/egusphere-2026-1741
Preprint. Discussion started: 1 June 2026

2.1 KAIRA observations

2.1.1 VHF measurements

KAIRA (Kilpisjärvi Atmospheric Imaging Receiver Array) is a phased-array passive radio receiver, located at $+69.07°$ N, $+20.76°$ E, 523 m (GRS altitude), near Kilpisjärvi in northern Finland. It makes extensive use of the LOFAR-design, including antennas, digital signal-processing hardware and software (McKay-Bukowski et al., 2015). The facility was originally built as a demonstrator for the EISCAT_3D system, but with the intention to test the use of LOFAR technology for other active and passive geophysical remote sensing experiments. Since then, the facility has been used for a broad range of observations from HF-radar reception for atmospheric chemistry (Chau et al., 2018), VHF incoherent scatter radar (Virtanen et al., 2014), solar radio physics (Pohjolainen et al., 2023), multi-frequency riometry (Kero et al., 2014), scintillation (Fallows et al., 2014) and astronomy, using very long baseline interferometry with other radio telescopes (McKay-Bukowski et al., 2015).

KAIRA comprises two antenna arrays; the low-band antenna (LBA) array covers an approximate frequency range of $8-80$ MHz and the high-band antenna (HBA) array covers a nominal $110-270$ MHz. Whilst both the LBA and HBA arrays were used in this experiment, only the results from the LBA array are presented here. The LBA array comprises 48 LBAs, each of which is a crossed inverted-V-dipole aerial, standing $1.8m$ tall, above a 3 m by 3 m steel grid ground plane. This is optimized for maximum sensitivity to electromagnetic fields from within zenith angles of $\pm 60°$. The dipole length is approximately 2.4 m and the wires are at a $45°$ angle with the vertical plastic centre pole. There is a separate amplifier/filter chain per dipole, producing two linearly polarised outputs per element.

An 8 MHz high-pass filter provides a hard limit to the lower edge of the observable frequency range, although shortwave radio transmissions extend up to 25 MHz and make observing difficult below this frequency (McKay, 2018). The antenna impedance varies from capacitive (short dipole approximation) to inductive (where the dipole is long compared to the wavelength) and is resonant at approximately 58 MHz (McKay et al., 2015). Antenna geometry, amplifier response and several filters result in a gradual decline at higher frequencies, effectively ending at 88 MHz, which is the start of the FM-radio band.

The antennas of the LBA array are arranged in a quasi-random pattern across a field approximately 34 m in diameter to give a synthetic beam profile with low sidelobes. The beam size is frequency dependent and, because of the fixed antenna locations, is subject to an elongation along the vertical axis for non-zero zenith angle, Z (McKay et al., 2015).

The antennas and signal processing are the same as a LOFAR station (van Haarlem et al., 2013). The signal received using each antenna polarisation is digitised, with a polyphase filter then dividing it into 512 channels (called “subbands”), each with a bandwidth of 195.3125 kHz (100 MHz total bandwidth across the band). A digital beamformer can use up to 488 of these

https://doi.org/10.5194/egusphere-2026-1741
Preprint. Discussion started: 1 June 2026

subbands (with 8-bit digitisation) to produce multiple synthesised beams, each in an arbitrary direction. For this study, the system was configured to produce a single beam in the direction of Cas A, using 488 subbands for a total bandwidth of 95 MHz. Statistics data were recorded with a time cadence of 1 s for visualisation purposes, but 100 Hz cadence data were also recorded using the main station output data stream. Given that ionospheric scintillation tends to occur over lower spectral frequencies (examples can be found in Fig. A1 and Fig. A2), higher rates (whilst possible) were not used for this experiment, hence keeping the data volume to a reasonable level.

Additionally, a configurable single-frequency-channel correlator can produce a complex, covariance matrix for all antenna combinations in the array for one subband each second. This mode, the data from which are known as "cross-correlation statistics", was used to generate the data for all-sky imaging.

2.1.2 KAIRA VHF scintillation

Radio waves from Cas A were observed over a wider range of frequencies with both KAIRA LBA and HBA arrays. These observations were based on the estimate of the Stokes I parameter (Cas A is almost entirely unpolarised below 1 GHz), which estimates the intensity of the received radio waves at each observed frequency. In this experiment observation modes 3 and 5 were utilised, covering frequency ranges $10 - 90$ MHz and $110 - 190$ MHz.

The occurrence of intensity scintillation on these radio waves was estimated by means of the S_4 scintillation index defined as (Briggs and Parkin, 1963):

$$S_4 = \sqrt{\frac{\langle I^2 \rangle - \langle I \rangle^2}{\langle I \rangle^2}} \qquad (1)$$

where I is the intensity of a radio wave with a specific radio wave frequency, as received by KAIRA. The operation $\langle\rangle$ indicates ensemble averaging: in practice, this is substituted by temporal averaging over a suitable interval of time under the assumption of ergodicity (Forte et al., 2022; Flisek et al., 2023).

In order to remove trends and biases in the received intensity, the zero-mean normalised intensity was estimated from I: and then, the S_4 index was given by the standard deviation of the zero-mean normalised intensity over a suitable interval of time.

The interval of time over which the S_4 is estimated depends on the inertial subrange of the intensity fluctuations originated (through a scattering-like process) by fluctuations in the spatial distribution of the plasma density (in this case within the ionosphere). Here, an interval of 3 minutes was utilised under the assumption of ergodicity (more details on this assumption

https://doi.org/10.5194/egusphere-2026-1741
Preprint. Discussion started: 1 June 2026

can be found in Forte et al., 2022 and Flisek et al., 2023). The 3 minutes interval appeared to be sufficient for most observing conditions within this experiment to capture enough fluctuations through the S_4 index; however, in some cases (e.g., 25 November 2011 around 19:30 – please see section 3) the scintillation timescale appeared to be somewhat longer, hence introducing larger uncertainties in the S_4 estimate.

The S_4 scintillation index was estimated for all the radio waves intensities with frequency in both the LBA and HBA ranges (although only LBA results are shown here).

2.1.3 All-sky imaging

KAIRA recorded cross-correlation statistics with a time resolution of $1s$ at the frequency of 70.3 MHz in order to produce all-sky images. The observations carried out within this experiment were arranged into one hour intervals, to prevent the recorded data files from becoming unwieldy. In order to produce an image of the sky, a calibration of the values observed by each antenna was carried out by applying gain coefficients to a complex covariance matrix (McKay et al., 2015).

The calibration procedure was accomplished on summed XX and YY polarisation and the resulting matrix was then transformed into a 150-by-150 pixels visibility function $V(u,v)$. From the visibility function $V(u,v)$(Van Cittert-Zernike Theorem) the distribution of the intensity in the (l,m) plane, $I(l,m)$, can be estimated as (van Cittert, 1934; Zernike, 1938; McKay, 2018):

$$V(u,v) = \iint I(l,m)e^{-2\pi i(ul+vm)}dldm \qquad (2)$$

which is the Van Cittert-Zernike Theorem relating the visibility function $V(u,v)$ to the the intensity distribution $I(l,m)$ across the (l,m) plane (all sky).

https://doi.org/10.5194/egusphere-2026-1741
Preprint. Discussion started: 1 June 2026

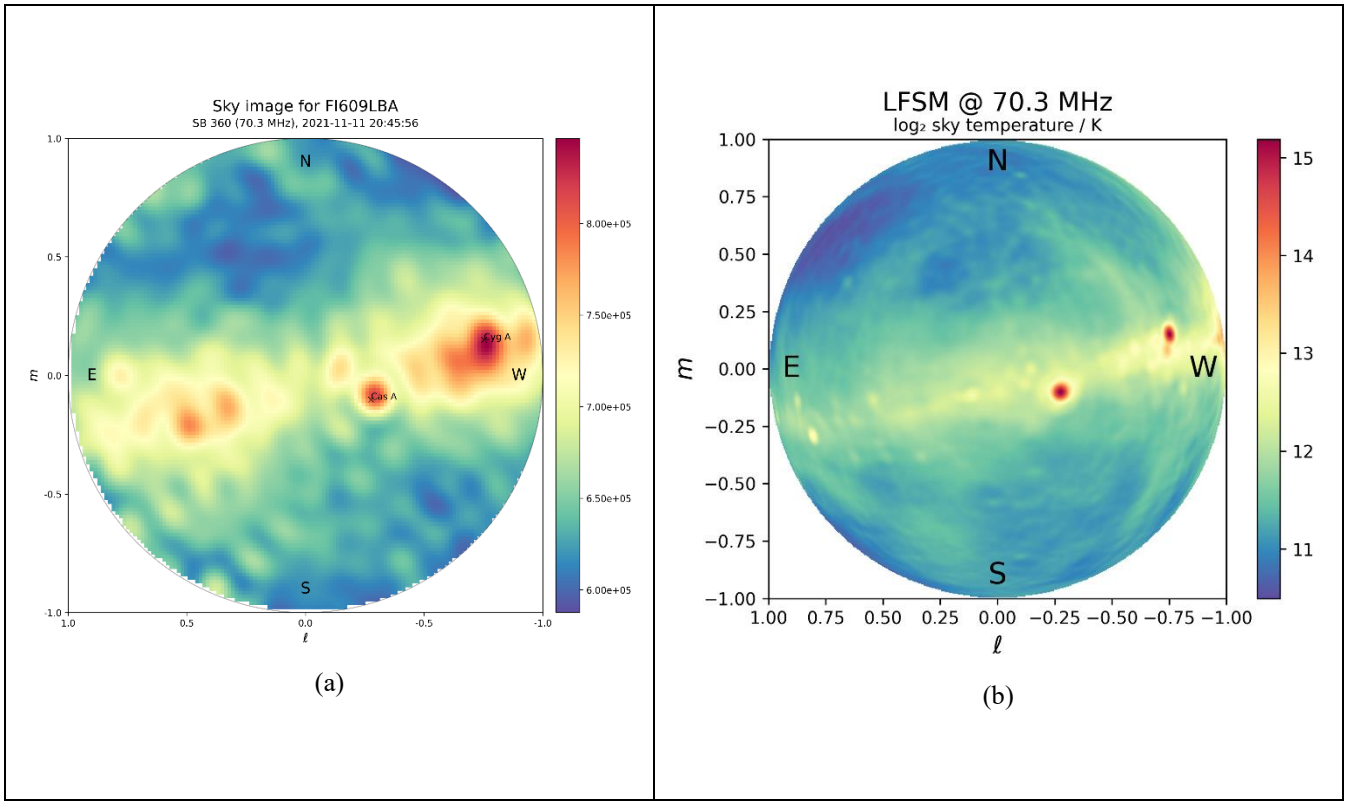

265 **Figure 2:** (a) A representative single frame of all-sky $I(l,m)$ observations collected throughout this experiment. The single frame refers to 11 November 2021 20:45:56 UTC. The spatial resolution of this type of images is approximately of the order of 7°. The colour scale is in raw ADU units from the instrument. The entire sequence of all-sky images can be appreciated through the animations provided as supplementary material. (b) The all-sky model of Dowell et al. (2017), interpolated to 70.3 MHz in the same projection as Fig. 2(a) (units of K).

270

A representative example of an all-sky image $I(l,m)$ is illustrated in Fig. 2, where the colour scale is in raw ADU units from the instrument. The point with coordinates $(0,0)$ represents the zenith whilst the horizon is the circle defined by $l^2 + m^2 = 1$. The Eastern and Northern components of the angular distance from the zenith are given by $sin^{-1}(l)$ and $sin^{-1}(m)$ respectively; i.e. an orthographic projection (e.g. Calabretta & Greisen 2002). An orthographic projection is used in Fig. 2,
275 which projects the sky to a tangent plane on the celestial sphere, centred at zenith. This compensates for the $sec(Z)$ beam-elongation of a fixed interferometer in the horizontal plane (McKay, 2018, Fig.5.1). The projected spatial resolution of this type of all-sky images collected during the experiment by means of KAIRA is equivalent to approximately 7° (McKay-Bukowski, 2015, Fig.8; McKay, 2018). Fig. 2(b) shows the same sky generated from the LWA-1 Low-frequency Sky Survey of Dowell et al. (2017) using pyGSDM (Price, 2016). The two images have obvious commonalities in their brightest sources

https://doi.org/10.5194/egusphere-2026-1741
Preprint. Discussion started: 1 June 2026

and the location of the diffuse structure associated with the Galaxy. There are some differences also. The resolution of the LFSS is somewhat higher, and the narrowband snapshot KAIRA image is stippled due to the sidelobes of the PSF. Another difference between the KAIRA snapshot image and the sky model is the presence of an omnipresent flux completely covering the sky. Since this flux is missing from the Low-frequency Sky Survey, which was produced carefully by measuring the zero-spacing flux and by controlling for the effects of mutual coupling between dipoles, it is plausible that this background flux can be ascribed to an instrumental effect. The temporal variation of all-sky images collected throughout this experiment can be appreciated in the animations provided as supplementary material (accessible at https://zenodo.org/records/18986049?preview=1&token=eyJhbGciOiJIUzUxMiJ9.eyJpZCI6ImVmOTMxN2MyLWFiYjUtNGQ1MC1iNjRhLWFjZDg2YzM1MTgxYSIsImRhdGEiOnt9LCJyYW5kb20iOiIwMmViMzcyNGJkNGYwMDkzNzNkYjUzZTEwNGEwYzlhOSJ9.Zbkj9LyU4eE_u_qUmoNMiuK4gtR_Y8cVmf7B2VZMdiYNBfl3ZrGFEYbvG_-sxjrPTBbWFNxN8UuyH0dTDazt8A).

From the all-sky images, taken simultaneously with the beam-formed scintillation observations, attention was narrowed to a smaller area encompassing only the Cas A source. A new image zoomed around Cas A was calculated by using the overall intensity distribution function (Eq. (2)): this new zoomed image of the source covers an area of approximately 36° in both directions (i.e., $-18°$ to $+18°$) from the coordinates of the source centre (Fig. 3(a)). A new set of (l, m) coordinates were defined to describe the source-zoomed image and were expressed in degrees (Fig. 3(b-f)).

The zoomed image of the source can be characterised by fitting a suitable two-dimensional function to the source-zoomed image and by observing how this fitted function (and its parameters) vary over time. To this purpose, the intensity $I(l, m)$ distributed across all the source-zoomed image was divided by its median value. Then, the source-zoomed image was discretised by means of 150-by-150 pixels and a two-dimensional gaussian function was fitted to the pixelated version of the original source-zoomed image resulting from the measured visibility function.

Figure 3(a) illustrates the principle of the source-zoomed image: a gaussian fitting was applied across the fitting area corresponding to the (l, m) area enclosing the Cas A source (Tong, 1990). Figures 3(b-f) illustrate the concept of the 2D gaussian fit on the pixelated version of the source-zoomed image, by means of white contour isolines.

https://doi.org/10.5194/egusphere-2026-1741
Preprint. Discussion started: 1 June 2026

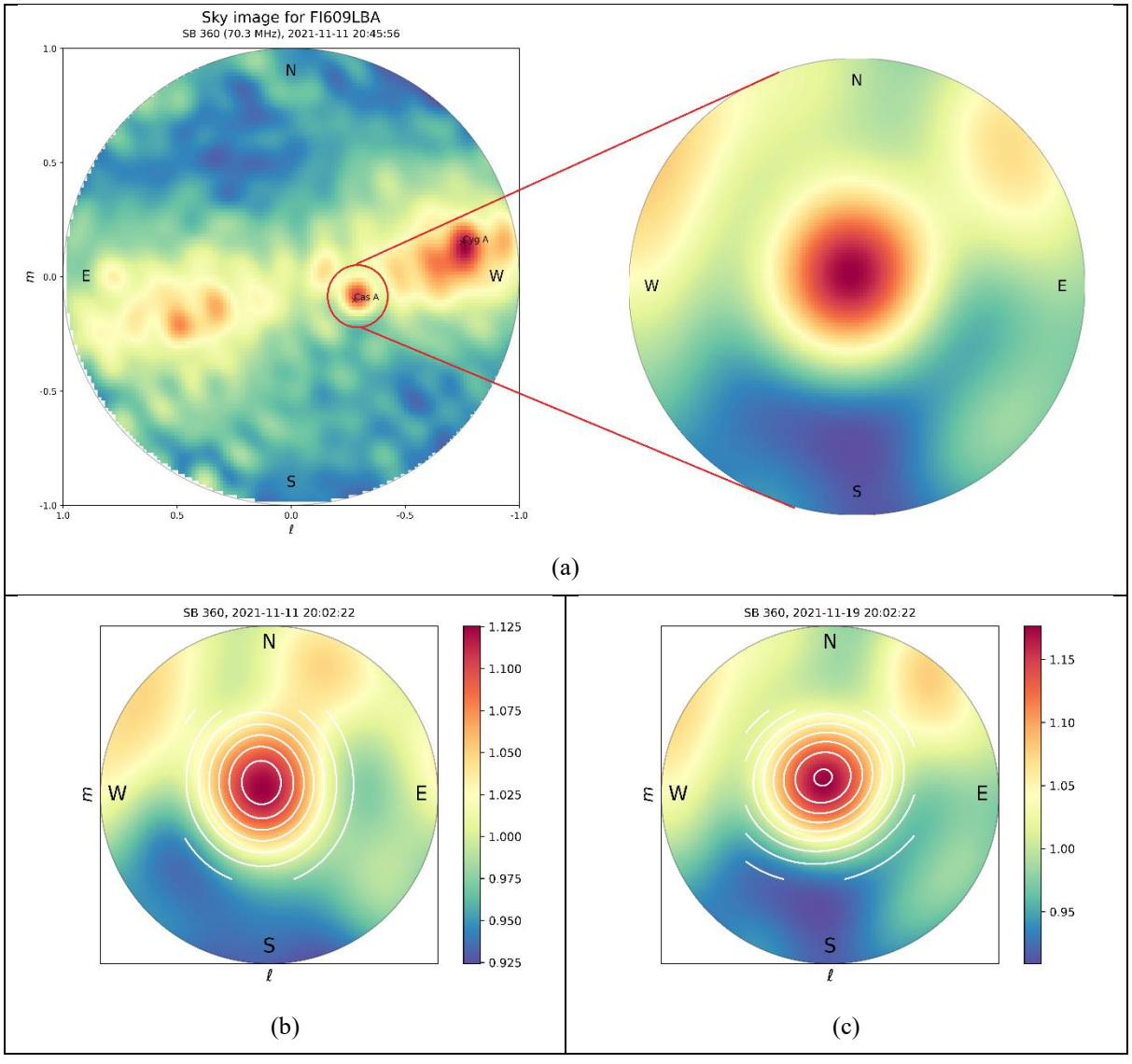

https://doi.org/10.5194/egusphere-2026-1741
Preprint. Discussion started: 1 June 2026

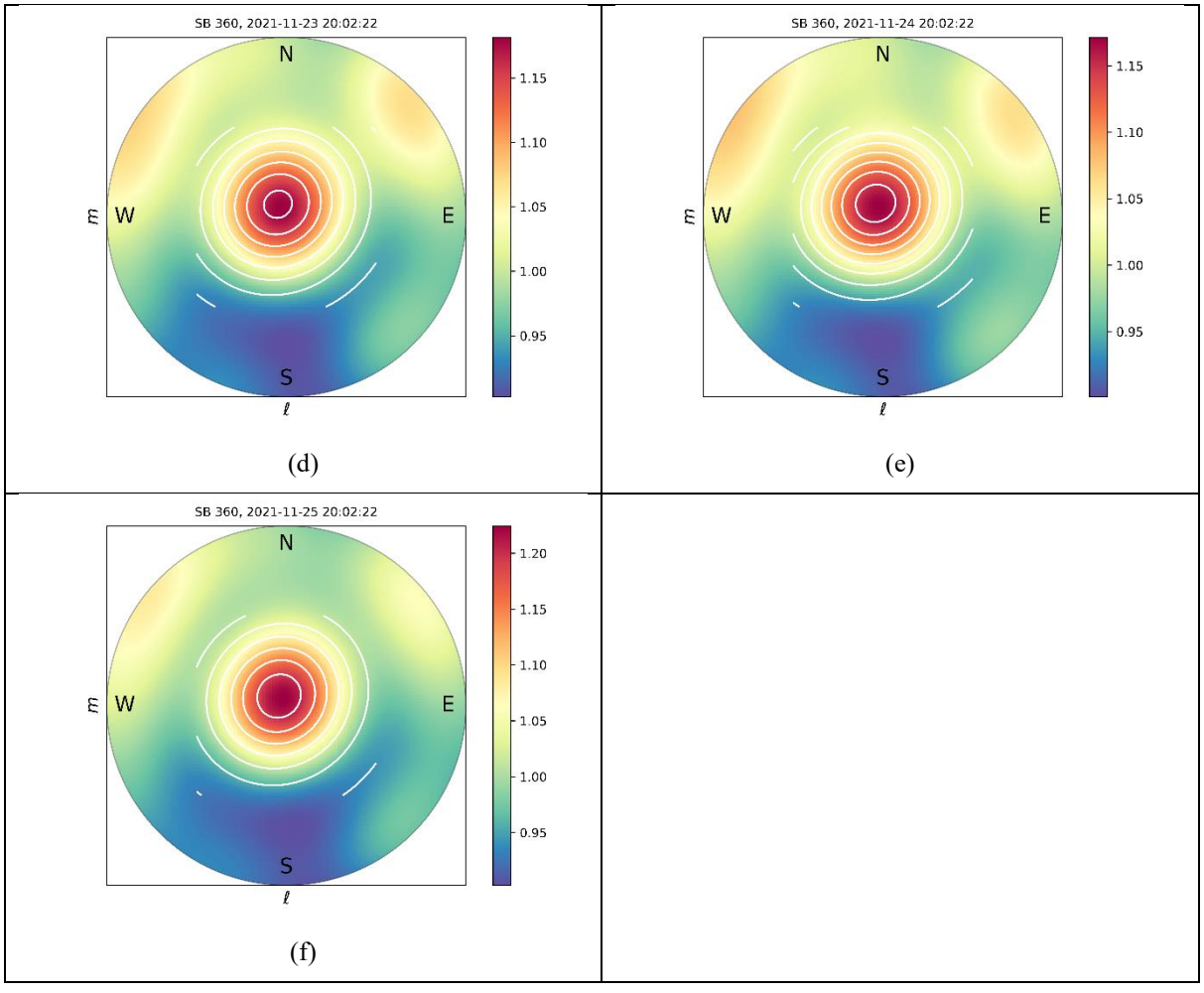

Figure 3: Representative examples of the source-zoomed imaging for Cas A based on KAIRA all-sky images recorded in all available days of the experiment. (a) The area from the all-sky image that was utilised to estimate a source-zoomed image. The imaging of the source was limited to an area surrounding the Cas A source extending approximately 18° in all directions from the source centre. (b-f) White contour isolines illustrate a two-dimensional gaussian best-fit of the shape and intensity of the source. The concept of the source image fitting is illustrated for the same time in different days during the experiment: (a) 11 November 2021, (b) 19 November 2021, (c) 23 November 2021, (d) 24 November 2021, (e) 25 November 2021. Each of the fits refer to the same hour, 20:02:22 UTC. The complete variation of the source imaging can be appreciated by means of animations covering the entire duration of the experiment in each day, available as supplementary material.

A new set of (l, m) coordinates was considered with origin at the nominal astronomical position of the Cas A centre (l_0, m_0) for each image collected every second. However, the 2D gaussian fit was specified in the new coordinates (x, y) which are

https://doi.org/10.5194/egusphere-2026-1741
Preprint. Discussion started: 1 June 2026

rotated from the source-centred coordinates by an angle θ (Fig. 4) to account for any rotation in the source image (the angle θ was estimated within the fit). The origin of the (x, y) coordinates ((0,0) or (l_0, m_0) in (l, m) coordinates) is at the nominal astronomical position of the source: however, the centre of the gaussian fit may differ from the nominal astronomical position of the Cas A centre (i.e., the origin of the new (x, y) coordinates at each second), for example, as a consequence of ionospheric refraction. Fig. 4 illustrates the relation between the rotated (x, y) coordinates and the source-centred (l_0, m_0) coordinates together with the various levels of the 2D gaussian fit (red ellipses).

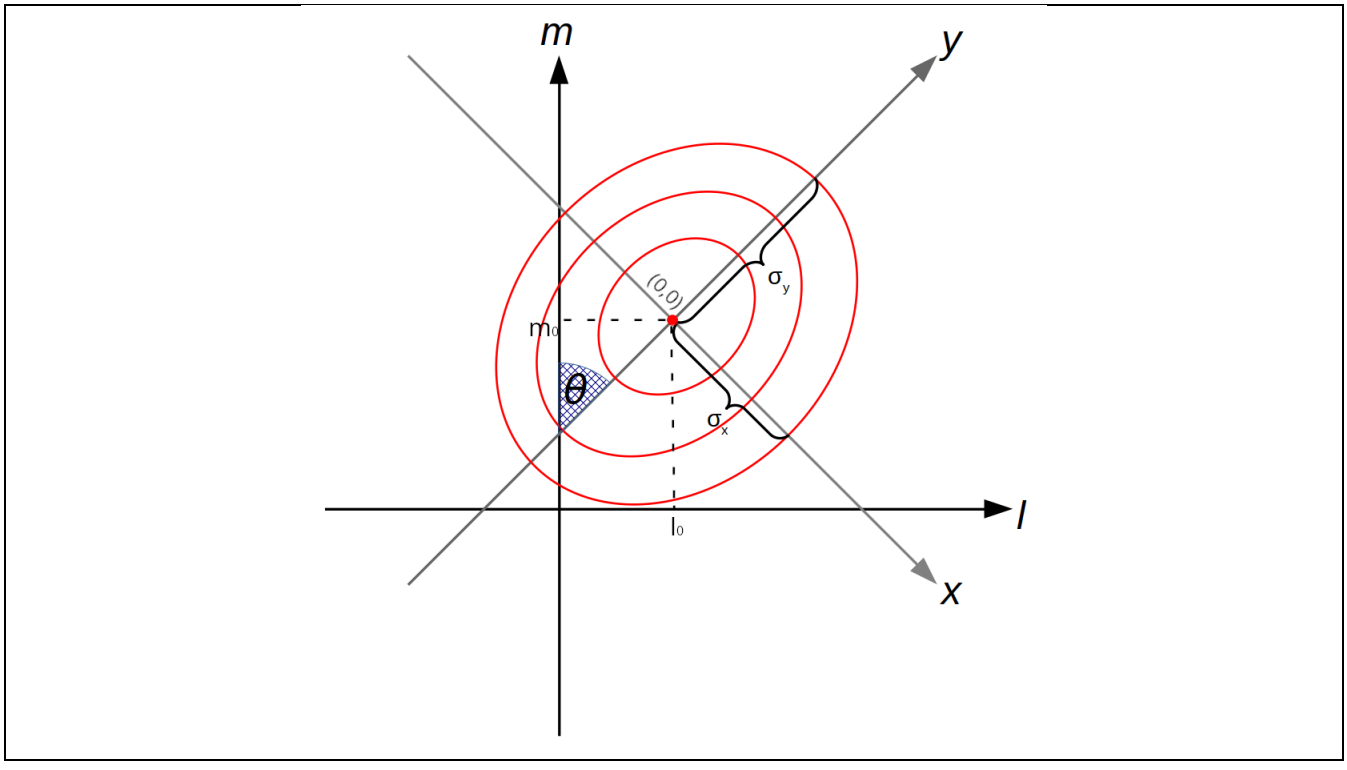

Figure 4: The relation between the (l, m) and (x, y) coordinates. The concentric red ellipses represent the various levels of the 2D gaussian fit (these are purely illustrative and do not correspond to 1-, 2-, 3-sigma levels).

The image area around the Cas A source to be fitted contains the same number of pixels as an all-sky image. Within the specified fitting area, the two-dimensional gaussian function given by (Fig. 4):

$$f(x, y) = B + A \cdot exp\left(-(a(x - x_0)^2 + 2 \cdot b(x - x_0)^2 + c(y - y_0)^2)\right) \quad (3)$$

was fitted to the image area by applying a non-linear least squares method (Kariya and Kurata, 2004), with a, b, c defined as:

https://doi.org/10.5194/egusphere-2026-1741
Preprint. Discussion started: 1 June 2026

$$a = \frac{cos^2\theta}{2 \cdot \sigma_x^2} + \frac{sin^2\theta}{2 \cdot \sigma_y^2} \qquad (4a)$$

$$b = \frac{sin\theta \cdot cos\theta}{2 \cdot \sigma_x^2} + \frac{sin\theta \cdot cos\theta}{2 \cdot \sigma_y^2} \qquad (4b)$$

$$c = \frac{sin^2\theta}{2 \cdot \sigma_x^2} + \frac{cos^2\theta}{2 \cdot \sigma_y^2} \qquad (4c)$$

In Eq. (3), A is the amplitude of the gaussian function (fitting normalised intensity across the source-zoomed image) and B is an offset term that accounts for any varying background in the source-zoomed image (as much as possible). The gaussian fitting was performed for all images, i.e. one every second over the observation period. The area of the (l, m) plane corresponding to the source-zoomed image was somehow wider than the area occupied by Cas A: this was necessary to retain most of the 2D gaussian function, hence preserving the goodness of the 2D fit. This implied that the area over which the 2D gaussian fit was applied had to extend over at least 3 standard deviations in order to fit most of the 2D gaussian function (Tong, 2012). Hence, the area corresponding to the source-zoomed image extended over approximately 18° in all directions from the coordinates of the source centre: that is, slightly beyond the 3 standard deviations.

From this 2D gaussian fit, adapted to the source imaging typical of a radio telescope observation, various parameters characterising the source were estimated every 1 s (i.e., for each image measured). These parameters include the source centre intensity brightness (which is the intensity from the visibility equation divided by its median value), the displacement of the source centre from its nominal position in the (l, m) plane (in degrees) and the standard deviations along two directions (σ_x and σ_y in the rotated (x, y) plane) (in degrees): the best fit is indicated by means of white lines in Fig. 3 (red lines in Fig. 4) and in the corresponding supplementary animations (where frames update every minute instead of every second for simplicity). Hence, the temporal variation of the fitting parameters can be utilised to infer properties of the ionospheric propagation medium. Due to the finite resolution of the instrument, a point source will appear as an elliptical Gaussian in these images. An important feature of this orthographic projection is that the shape of this elliptical Gaussian in (l, m) coordinates is constant over the whole sky. The target source will move in (l, m) coordinates as the Earth Rotates (in a predictable way). Any other change in location or change in shape or brightness of the source can be ascribed to ionospheric effects: in the absence of ionospheric (or instrumental) effects, the fitted parameters are expected to remain constant

https://doi.org/10.5194/egusphere-2026-1741
Preprint. Discussion started: 1 June 2026

The imaging of the source Cas A reveals temporal variations in its brightness at the centre, displacements of the position of its centre from the nominal source position, and variations in the shape of the source. The magnitude of these changes varied throughout the observation periods and can be appreciated in full through animations available as supplementary material.

In order to encapsulate the variations of the source image a new function that combines the temporal behaviour of the gaussian fit parameters is proposed as:

$$\beta(t) = \beta_I(t) + \beta_D(t) + \beta_\sigma(t) \qquad (5)$$

where the three terms in Eq. (5) are defined as follows.
In relation to the gaussian source centre intensity I, it is possible to consider:

$$I(t) = \frac{I(t)}{\langle I(t)\rangle} - \langle\frac{I(t)}{\langle I(t)\rangle}\rangle \qquad (6)$$

which gives a zero-mean normalised estimate of the gaussian source centre intensity, where $\langle\rangle$ indicates a temporal moving average over 180 s (3 minutes). The function $\beta_I(t)$ is given by:

$$\beta_I(t) = \sqrt{\frac{I^2 - \langle I\rangle^2}{\langle I\rangle^2}} = \sqrt{[I(t)]^2 - \langle[I(t)]\rangle^2} = \sigma_{I(t)} \qquad (7)$$

The function $\beta_I(t)$ describes the fluctuations in the source centre intensity (or brightness) in a fashion similar to the S_4 scintillation index. It can be observed (Fig. 7 in relation to the source centre intensity) how the variations in $\beta_I(t)$ are larger than the S_4 index estimated through KAIRA VHF beam-formed scintillation measurements. The S_4 estimates based on beam-formed observations are affected by the source extension whereas the source image is obtained from the visibility function.

In relation to the displacement D of the source centre from its nominal position (as deduced from the gaussian fit), the function $\beta_D(t)$ given by:

$$\beta_D(t) = \frac{D}{1 + D} \qquad (8)$$

https://doi.org/10.5194/egusphere-2026-1741
Preprint. Discussion started: 1 June 2026

where D was given in radians. The function $\beta_D(t)$ projects D into the [0,1] interval and describes variations in D by preserving trends (e.g., introduced by large scale ionisation structures) and fluctuations (due to scintillation introduced by small-scale irregularities).

In relation to the gaussian standard deviations (σ_x and σ_y), the function $\beta_\sigma(t)$ is given by:

$$\beta_\sigma(t) = \frac{\sqrt{\sigma_x^2 + \sigma_y^2}}{\sqrt{1 + \sigma_x^2 + \sigma_y^2}} \quad (9)$$

where σ_x and σ_y were expressed in radians. The function $\beta_\sigma(t)$ combines the contributions from both σ_x and σ_y and projects them into the [0,1] interval, by preserving trends and fluctuations. Each term in Eq. (5) saturates around or approaches asymptotically 1: hence their sum should saturate around or approach asymptotically 3 in the presence of strong scintillation and strong trends. Figure 8 illustrates the function $\beta(t)$ together with its three components during each of the days considered.

2.2 EISCAT Observations

In order to identify and characterise ionospheric structures occurring in the auroral ionosphere and originating propagation effects (both on KAIRA VHF observations and on L-band GNSS observations) electron density (N_e) profiles were measured by means of the EISCAT UHF ISR in Tromsø (Jakowski et al., 1996; Forte et al., 2013; Forte et al., 2017). Since KAIRA was observing radio wave scintillation occurring on radio waves received from Cas A, the EISCAT UHF ISR was set to follow Cas A throughout the duration of the allocated measurement time, thus providing electron density profiles along directions towards Cas A. Electron density profiles were calculated by using a 60 s integration time (Forte et al., 2013; Forte et al., 2017; John et al., 2021a; John et al., 2021b): other parameters, such as ion and electron temperature, can be estimated (although these are not shown here). The EISCAT Svalbard Radar (ESR) simultaneously measured electron density profiles along the same constant direction of the magnetic field line (i.e., field-aligned). ESR field-aligned observations can show evidence of equatorward moving plasma structures (in case of any) appearing first at ESR and then over EISCAT in Tromsø. More in general, ESR observations provide further context on the ionospheric conditions during the experiment.

During the experiment which took place across several days in November 2021, adverse meteorological conditions caused mechanical difficulties which limited the operation of the single-dish ESR antenna and then disruptions to the EISCAT UHF observations: as a consequence, only a subset of measurements was ultimately available from the days originally planned. Dates and times of the measurements carried out are listed in Table 1, together with a summary of the main points of a particular observation, thus identifying the most interesting case studies.

https://doi.org/10.5194/egusphere-2026-1741
Preprint. Discussion started: 1 June 2026

Given that KAIRA and EISCAT are not co-located (separated by a distance of approximately 85 km) a separation between the Cas A-KAIRA ray paths and EISCAT beams was inevitable. The separation distance between ray paths in the E region and the F region was approximately comparable with the distance between the two instruments (assuming that the beams from the two instruments have the same geometry), thus leading to a reduction in the resolution of ionospheric irregularities originating specific propagation disturbances. A number of different GNSS ground stations in the surrounding of KAIRA, EISCAT, and ESR were considered for the estimate of the rate of change of TEC (ROT) during the EISCAT/ESR/KAIRA experiment. Whilst the IGS ground station KILP is very close to KAIRA, in general GNSS ray paths from the various ground stations considered were not co-aligned with EISCAT/ESR beams and with KAIRA-Cas A ray paths due to the geometry of GNSS satellites. However, observations from these GNSS ground stations as well as from ESR were considered to provide more context on the ionospheric conditions in the region surrounding EISCAT beams and KAIRA-Cas A ray paths during the experiment.

By inspecting evidence available from the network of SuperDARN radars (available at https://superdarn.ca/, details not shown here), both EISCAT and KAIRA measurements appeared to be at the equatorward edge of a 2-cell potential system and of the auroral oval, moving in and out of this system with time. The Tromsø dynasonde results appeared to suggest (not shown here) the possible presence of a horizontal plasma drift, approximately between $100 - 300$ m s^{-1} during the observations, although this estimate is at a very low confidence.

2.3 GNSS observations

Global Navigation Satellite Systems (GNSS) are based on L band radio signals transmitted by satellites in Medium Earth Orbit (MEO). Through the combination of GNSS observables (carrier phases and/or pseudoranges) observed over two different carrier frequencies it is possible to estimate the slant TEC (over a specific ray path between a ground station and a given GNSS satellite): a weighted average of slant TEC values from all the available GNSS satellites provides an estimate of the vertical TEC (VTEC) along the zenith of a given station (Leick et al., 2015). The slant TEC (STEC) can be estimated from the geometry-free combination of carrier phases over two different frequencies (at L band from different constellations) (Wanninger, 1993; Pi et al., 1999).

When utilising observations of STEC the ionosphere is typically described as a single, infinitesimally thin layer (or shell): STEC values are then localised at the intersection points between satellite ray paths (line of sight) and the ionospheric shell (ionospheric pierce points, IPPs). This is a mathematical abstraction that is useful for the visualisation of the bulk of ionisation. An additional ionospheric parameter is the rate of change of TEC (ROT) (Wanninger, 1993; Pi et al., 1999; Kotulak et al., 2020; John et al., 2021a; John et al., 2021b; Kotulak et al, 2021; Flisek et al., 2023; Forte et al., 2024). Considering 30 s RINEX observation files, at each available epoch t_k ROT is calculated as:

https://doi.org/10.5194/egusphere-2026-1741
Preprint. Discussion started: 1 June 2026

$$\mathrm{ROT}(t_k) = \frac{STEC(t_{k-1}) - STEC(t_{k+1})}{\Delta t} \quad \left[\frac{\mathrm{TECU}}{\mathrm{min}}\right] \qquad (10)$$

where $\Delta t = 1$ min and TECU $= 10^{16}$ el m^{-2}. Enhancements in ROT occur in the presence of large-to-small scale ionospheric irregularities, making ROT a useful detector of phase fluctuations induced by ionospheric irregularities. An elevation mapping (verticalisation) was further applied to the ROT values obtained from STEC estimates to reduce the elevation angle dependence.

Here, ROT values calculated on signals from different constellations at three different ground GNSS stations are considered: Kiruna (KIR0), Kilpisjärvi (KILP) and Ny-Alesund (NYAL). The first two ground stations are located in the surrounding of EISCAT UHF and KAIRA, whereas the last ground station is in the surrounding of ESR: these ground GNSS stations provide context about ionospheric conditions in terms of STEC temporal fluctuations (i.e., ROT). The GNSS data (RINEX files) are part of the International GNSS Service (IGS): RINEX data files were accessed through the IGS archive (https://cddis.nasa.gov/archive/gnss/products/) (Noll, 2010; Johnston et al., 2017).

3. Results

The results of the experiment are based on the comparison and combination of complementary observations carried out through different instruments: intensity scintillation observed by means of KAIRA on radio waves from Cas A, modelling of the Cas A source from all-sky images recorded with KAIRA, electron density profiles observed through the EISCAT UHF/ESR incoherent scatter radars, rate of change of TEC (ROT) observed from a number of ground IGS stations on GNSS ray paths sampling an ionospheric volume common to KAIRA and EISCAT observations.

A summary of the experiment is provided in Table 1.

Day	KAIRA	EISCAT	ESR	Comments
09 November 2021	-	✓	✓	No KAIRA data
11 November 2021	✓	✓	✓	Scintillation: low levels (Fig. 5-6) N_e: stable tenuous layer (Fig. 9) ROT: no enhancements (Fig. 11) Source image: low fluctuations, a weak trend at times (Fig. 7)
17 November 2021	✓	-	-	Mechanical problems

https://doi.org/10.5194/egusphere-2026-1741
Preprint. Discussion started: 1 June 2026

19 November 2021	✓	-	-	Mechanical problems
23 November 2021	✓	✓ (corrupted)	✓	Scintillation: higher levels (Fig. 5-6) N_e: some structures (Fig. 9) ROT: enhancements (Fig. 11) Source image: trends and higher fluctuations (Fig. 7)
24 November 2021	✓	-	✓	Scintillation: low levels (Fig. 5-6) N_e: some structures (ESR) (Fig. 9) ROT: no enhancements (Fig. 11) Source image: very low fluctuations, some trends (Fig. 7)
25 November 2021	✓	✓	-	Scintillation: higher levels (Fig. 5-6) N_e: Tenuous layer, with Es layer (EISCAT) (Fig. 9) ROT: small, localised enhancement (KILP) (Fig. 11) Source image: trends and fluctuations (Fig. 7)

Table 1: Summary of the observations carried out during the experiment. The last column contains a summary of the main aspects regarding each specific day of observations. The days containing comments in the last column provide the case studies considered here. "N_e" stands for electron density profiles.

https://doi.org/10.5194/egusphere-2026-1741
Preprint. Discussion started: 1 June 2026

3.1 KAIRA

Figure 5 shows zero-mean normalised intensity fluctuations at LBA observed in the various days of observation.

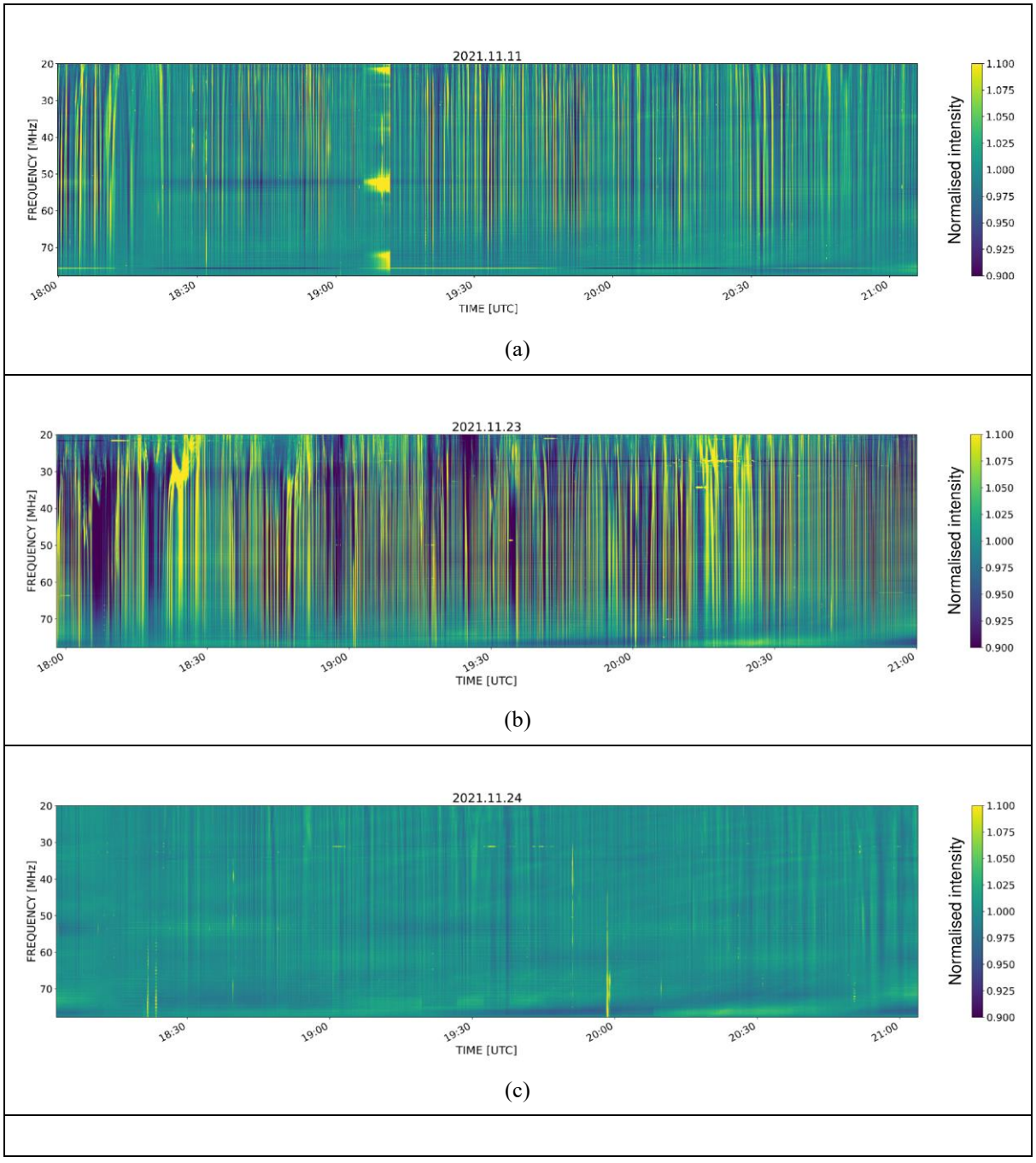

https://doi.org/10.5194/egusphere-2026-1741
Preprint. Discussion started: 1 June 2026

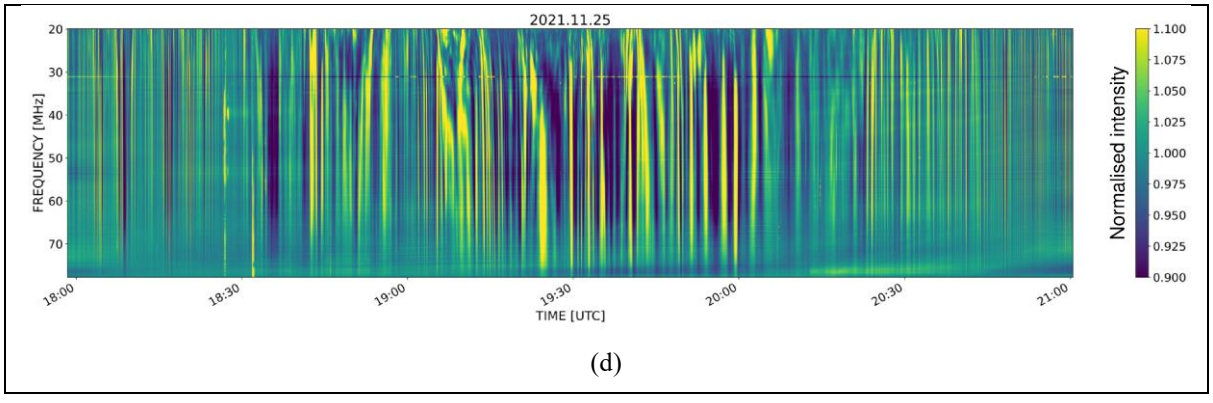

(d)

Figure 5: Zero-mean normalised intensity fluctuations for radio waves from Cas A as observed by KAIRA LBA. Here, results from (a) 11 November 2021 18:00-21:00 UTC, (b) 23 November 2021 18:00-21:00 UTC, (c) 24 November 2021 18:00-21:00 UTC, and (d) 25 November 2021 18:00-21:00 UTC, are illustrated.

Zero-mean normalised intensity fluctuations showed varying levels: for example, less pronounced at times on 24 November 2021 and more pronounced on 23 and 25 November 2021. Within the same day of observations, the scintillation activity varied in response to varying ionospheric conditions. Scintillation was recorded by means of the HBA part of KAIRA, as well: differences between LBA and HBA can be noticed, with scintillation activity generally lower at the higher radio wave frequencies of the HBA. However, due to corruptions in the observations the HBA part is not shown here.

https://doi.org/10.5194/egusphere-2026-1741
Preprint. Discussion started: 1 June 2026

Figure 6 shows the S_4 intensity scintillation index for LBA measurements in the various days of observation.

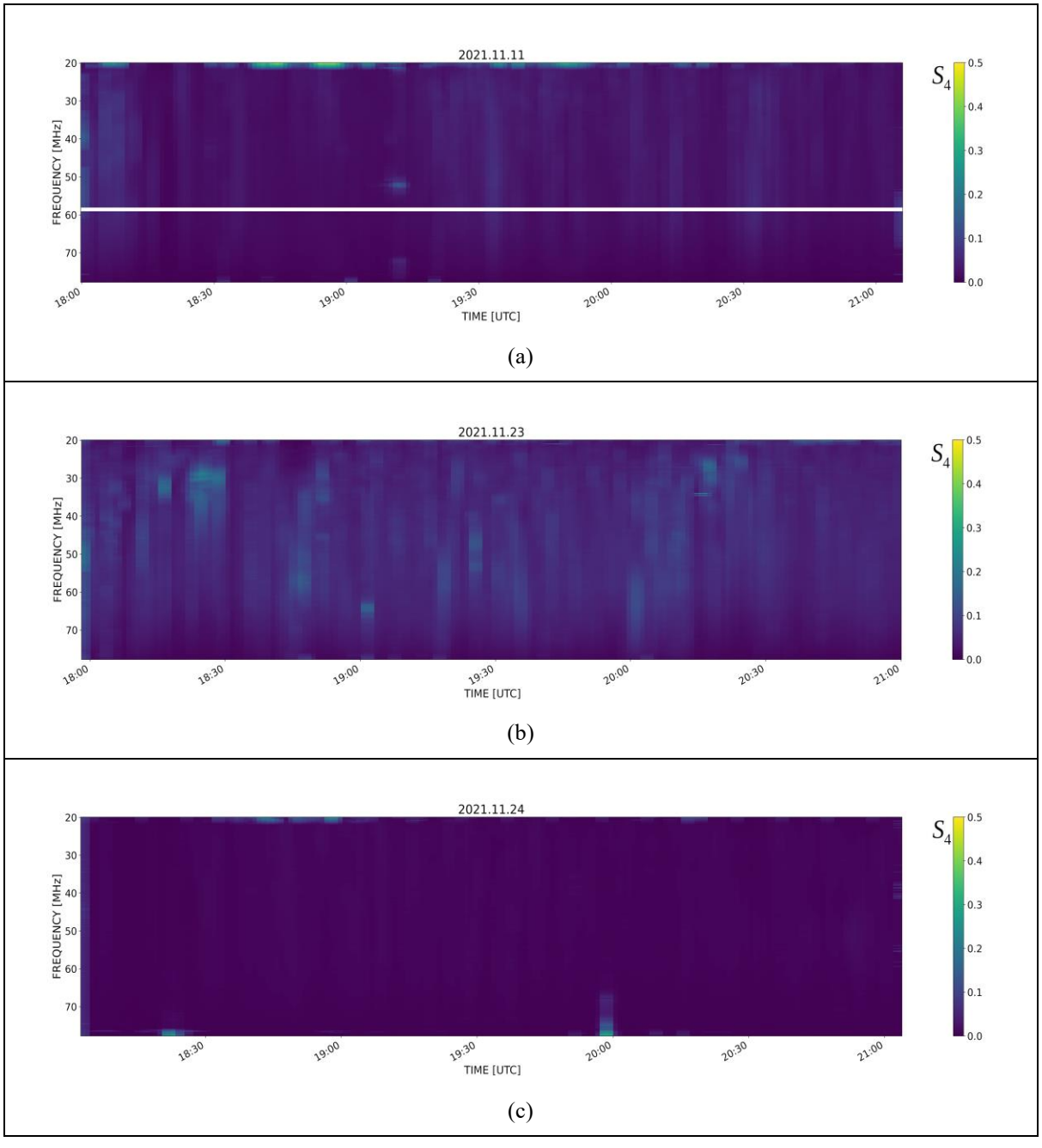

https://doi.org/10.5194/egusphere-2026-1741
Preprint. Discussion started: 1 June 2026

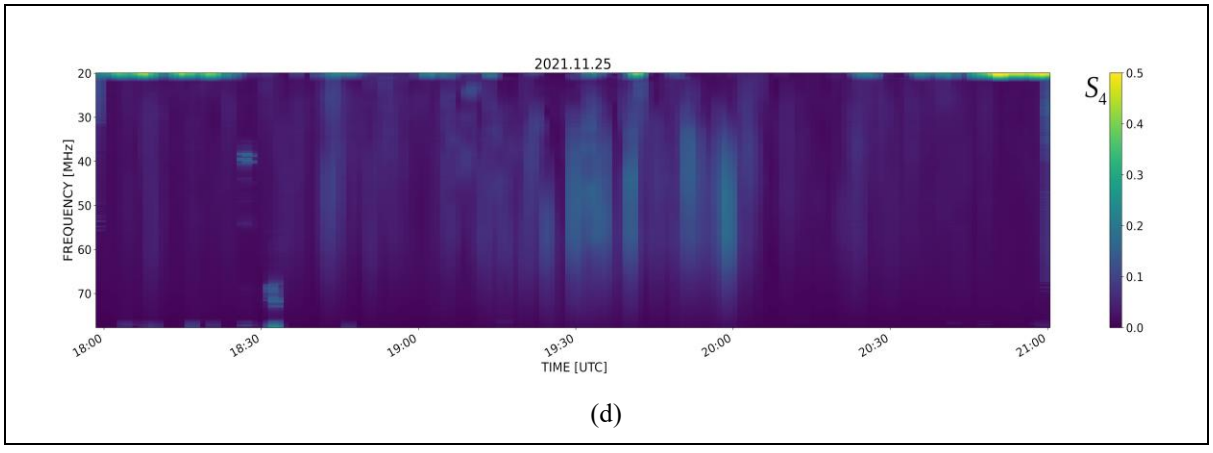

Figure 6: S_4 intensity scintillation index estimated for radio waves from Cas A as observed by KAIRA LBA. Here, results from (a) 11 November 2021 , (b) 23 November 2021, (c) 24 November 2021, (d) 25 November 2021 are illustrated.

It should be noted here that whilst 3 minute intervals appeared to be sufficient for most of the observing conditions, in some cases the scintillation timescale appeared to be somewhat longer: this requires a different time interval for the estimate of the S_4 index. In order to compare S_4 between different observations, the 3 minutes interval was utilised, noting that larger uncertainties may be possible in some cases (appendix A contains an additional analysis with a longer time interval). The main point to be noted here is in the zero-mean normalised intensity fluctuations (Fig. 5) which arise directly from small-scale irregularities in the inertial subrange – an indication of the spatial scales over which irregularities may form.

The source-zoomed image of Cas A (previously introduced in Figs. 3-4) was modelled by means of a 2D gaussian fit throughout the experiment in order to appreciate temporal variations related to the source more in detail. Figure 7 illustrates the variation of the main parameters of this fit: for each day, the intensity I of the source centre (i.e., the brightness of the central point of the source-zoomed image), the displacement D of the source centre from its nominal position (in degrees), and the standard deviations (σ_x and σ_y) as estimates for the half-widths of the 2D gaussian fit (in degrees) are illustrated as a function of time. The displacement D appears to show values smaller than the overall resolution in all-sky images achievable with KAIRA: this is due to the fact that the source-zoomed image was further discretised and pixelated. The 2D gaussian fit acts on this pixelated version of the source-zoomed image and estimates changes in the nominal position of the source centre as well as in the shape of the source. In all cases, some slower temporal trends are visible together with faster temporal fluctuations around a local average (the local average of the standard deviations reflects the source extension). The temporal fluctuations were observed to be more intense in some of the days (e.g., 23 and 25 November 2021) and quieter in other days (e.g., 11 and 24 November 2021).

https://doi.org/10.5194/egusphere-2026-1741
Preprint. Discussion started: 1 June 2026

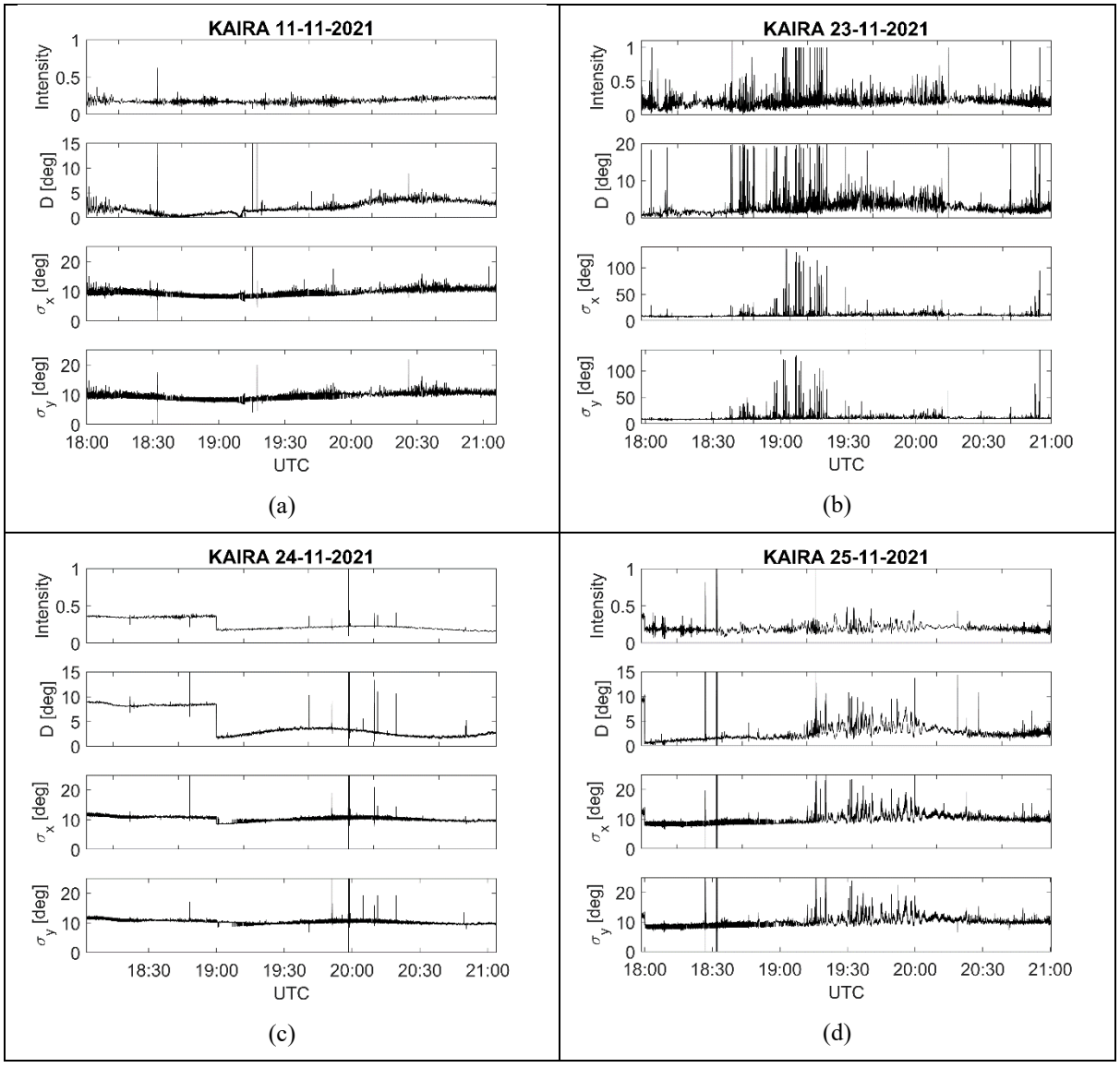

Figure 7: Gaussian fit parameters for Cas A images. The parameters are: the centre intensity (scaled by the median), the displacement D of the source centre from its nominal position (in units of degrees), and the standard deviations along x and y (in units of degrees). The plots refer to observations on 11 November 2021 (a), 23 November 2021 (with different vertical axes) (b), 24 November 2021 (where a jump approximately around 18:50 UTC occurred as a result of a change in the settings of the observations) (c), and 25 November 2021 (d).

Figure 8 shows the values of the β function as well as of its three components during each day of the experiment.

https://doi.org/10.5194/egusphere-2026-1741
Preprint. Discussion started: 1 June 2026

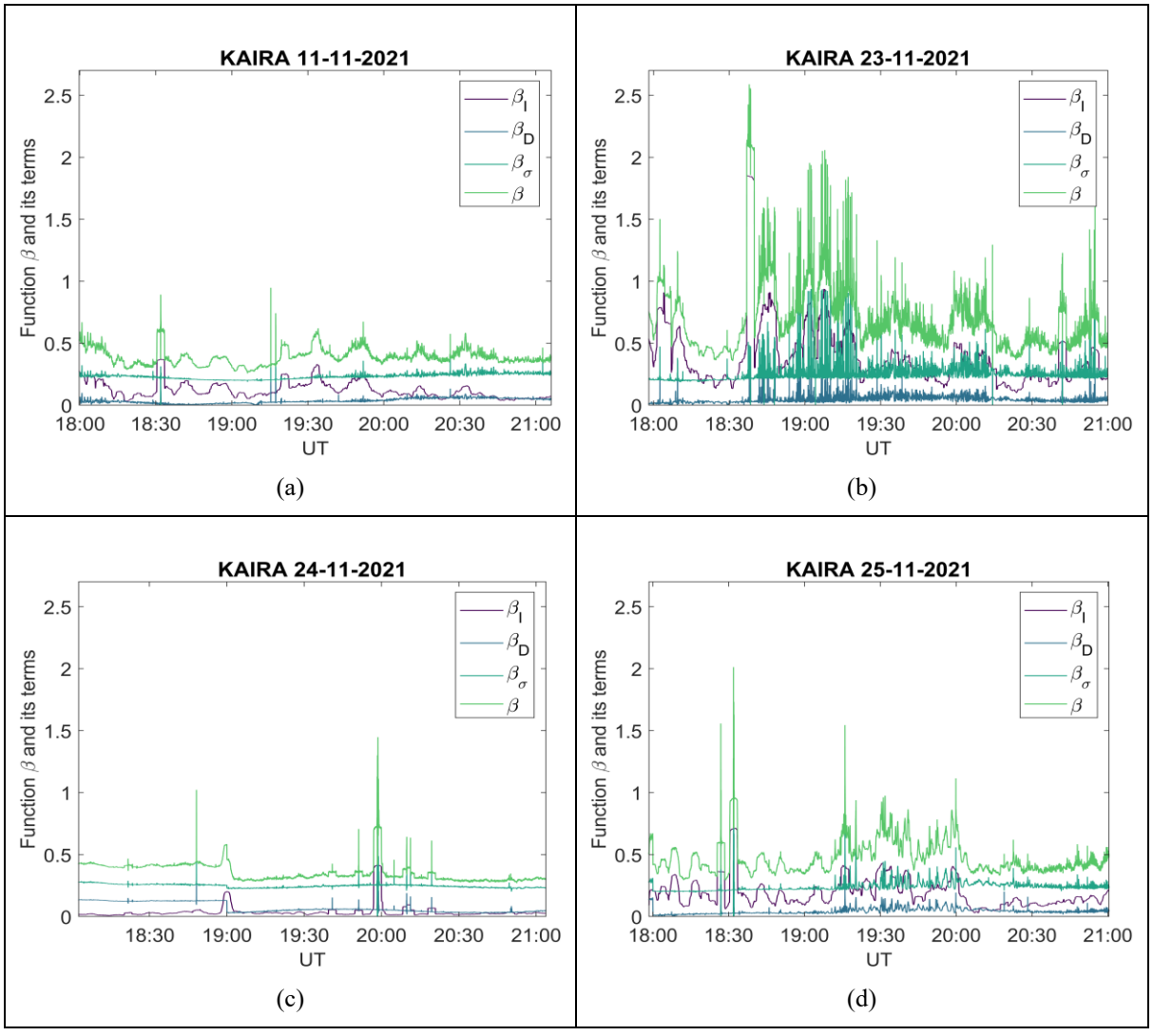

Figure 8: The β function summarising the variations in the fitted source-zoomed image, on the basis of a two-dimensional gaussian fit.

The values of the function $\beta(t)$ (dimensionless) vary with the different conditions in the ionosphere during the experiment. The fluctuations in $\beta_I(t)$ are more pronounced, for example, on 23 and 25 November 2021. On the other hand, $\beta_\sigma(t)$ shows an approximately constant average value with fluctuations around this value: the average value is a reflection of the source extension whereas the fluctuations around an average value are a consequence of degradations in the 2D gaussian fit due to

https://doi.org/10.5194/egusphere-2026-1741
Preprint. Discussion started: 1 June 2026

scintillation. Whilst in the case of KAIRA the capability of σ_x and σ_y is somewhat limited by the small array diameter, the concept in Eq. (5) and Eq. (9) can be generalised to larger and future arrays.

The function $\beta_D(t)$ varies from zero to positive values (a consequence of its definition), with slower trends and fluctuations: the trends away from zero appear to be consistent with a varying background ionisation (varying TEC) despite the change in elevation angle, whereas the fluctuations are due to scintillation which deteriorate the fit (areas of the sky adjacent to the source as well as noise become more prevalent, in an effect similar to optical blurring).

https://doi.org/10.5194/egusphere-2026-1741
Preprint. Discussion started: 1 June 2026

3.2 EISCAT

Figure 9 shows the electron density (N_e) profiles observed in the various days of observation, where EISCAT/ESR measurements could be collected.

555

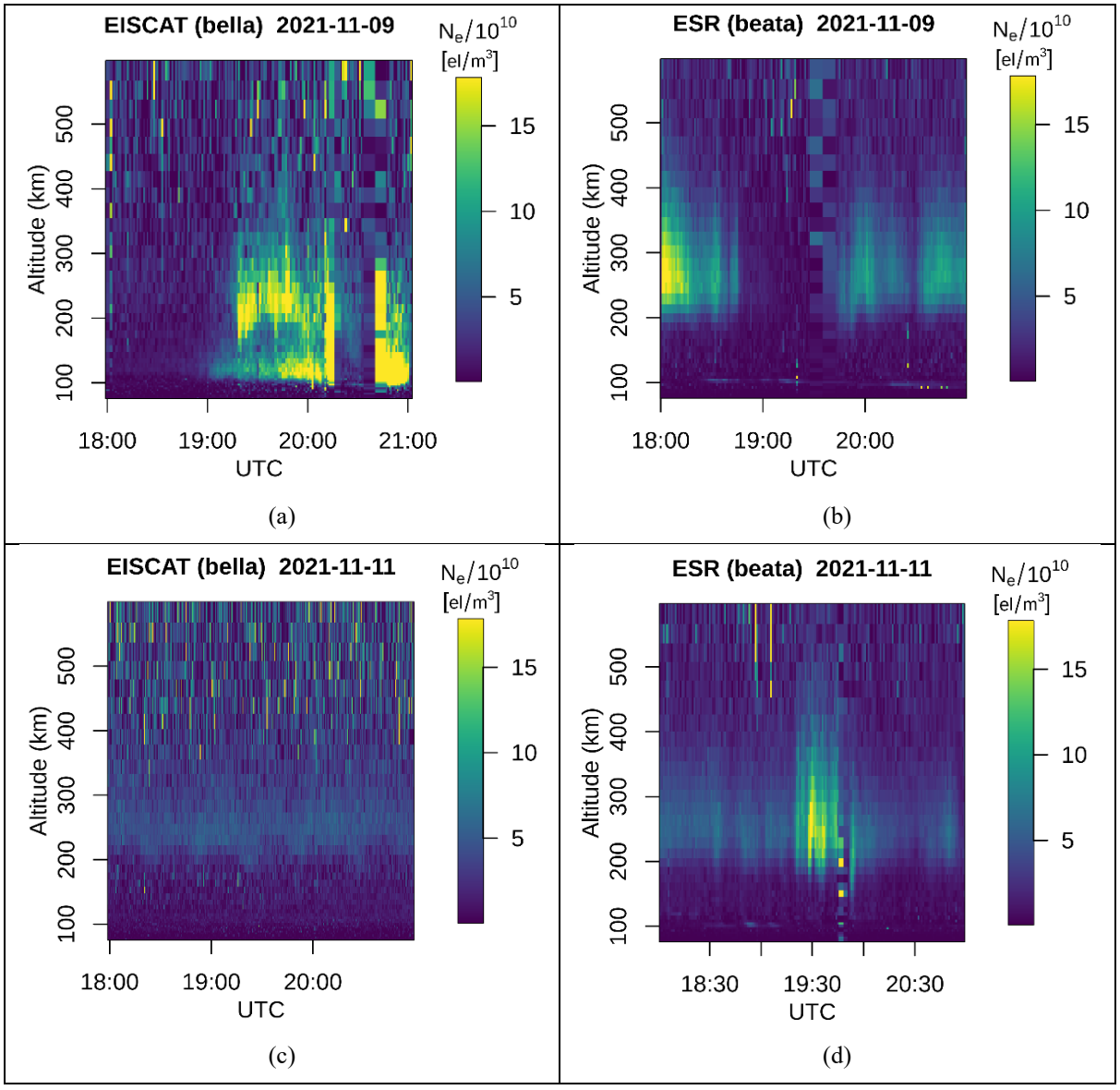

https://doi.org/10.5194/egusphere-2026-1741
Preprint. Discussion started: 1 June 2026

(observations corrupted) (e)	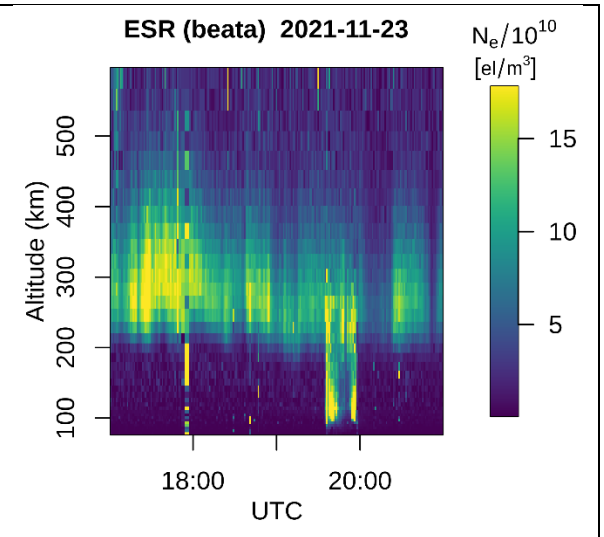 (f)
(mechanical problems) (g)	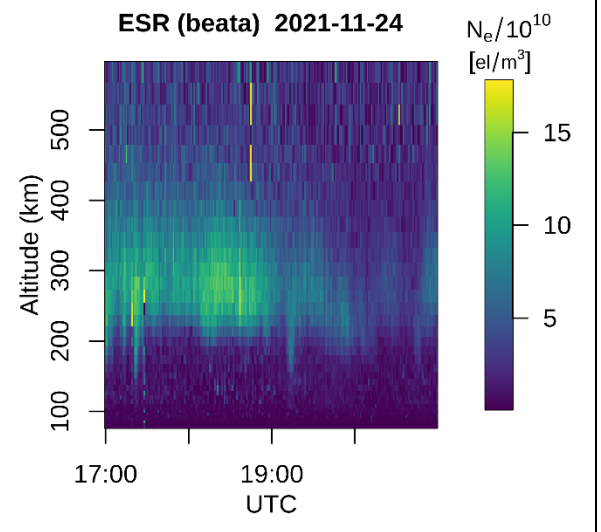 (h)

https://doi.org/10.5194/egusphere-2026-1741
Preprint. Discussion started: 1 June 2026

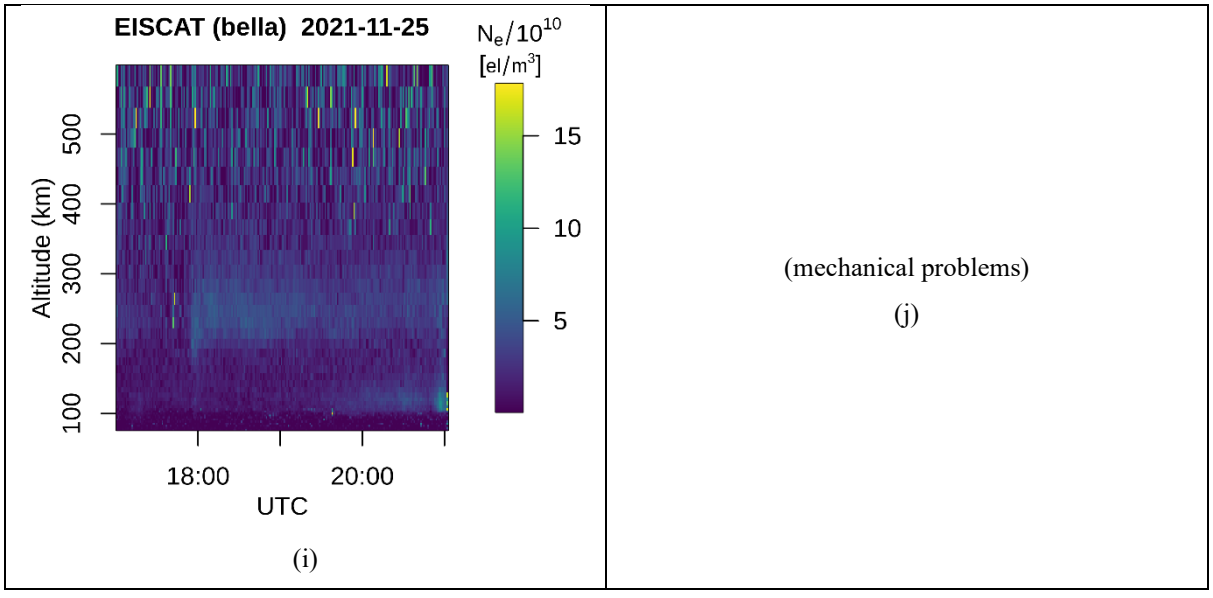

Figure 9: Electron density (N_e) profiles estimated through the EISCAT UHF/ESR incoherent scatter radars along directions to Cas A (same as KAIRA). Although measured along range, the electron density profiles are plotted as a function of altitude to deduce information on processes in different ionospheric regions. Here, results from (a-b) 09 November 2021 18:00:00-–21:00 UTC, (c-d) 11 November 2021 18:00-21:00 UTC, (e-f) 23 November 2021 17:00-21:00 UTC, (g-h) 24 November 2021 17:00-21:00 UTC, and (i-j) 25 November 2021 17:00-21:00 UTC are illustrated. EISCAT suffered mechanical difficulties preventing it from taking measurements in the other days scheduled.

Throughout the observations (Fig. 1), EISCAT detected enhancements in the electron density in both the F region and the E region. The interval of altitudes over which enhancements occurred varied, typically occurring over an interval approximately of the order of 100 km in the F region and approximately of the order of few tens of kilometres in the E region. The enhancement occurring in the E region on 25 November 2021 (Fig. 9(i)), between 20:00 UTC and 21:00 UTC is typical of a sporadic E layer. On the other hand, ESR observed generally more active conditions, with overall higher ionisation in the F region and ionisation gradients due to possible plasma patches (e.g., 11 November 2021) and particle precipitation (e.g., 23 November 2021).

In order to appreciate both bulk ionisation and ionisation gradients (responsible for trends and fluctuations, respectively, in the source fit parameters) within KAIRA's field of view, the EISCAT/ESR electron density profiles were integrated between approximately 100 km and 400 km of altitude (Jakowski et al., 1996; Forte et al., 2013; Forte et al., 2017), thus providing an estimate of the slant TEC along the radars' beams. Figure 10 illustrates the estimate of TEC for each electron density profile (approximately every $60s$) together with an estimate of the difference in TEC between consecutive profiles: the change in

https://doi.org/10.5194/egusphere-2026-1741
Preprint. Discussion started: 1 June 2026

TEC (ROT, in TECU min^{-1}) measured over approximately 60 s shows some similarities with the rate of change of slant TEC (ROT) deduced from ground GNSS receivers in the surrounding of EISCAT and ESR radars. In Fig. 10, both radar TEC and ROT are estimated either every 1 minute (red and cyan lines, respectively), or by means of an initial smoothing of TEC values aimed at reducing the noise through a 3-minute moving average (magenta and green lines, respectively) and through a 5-minute moving average (black and blue lines, respectively).

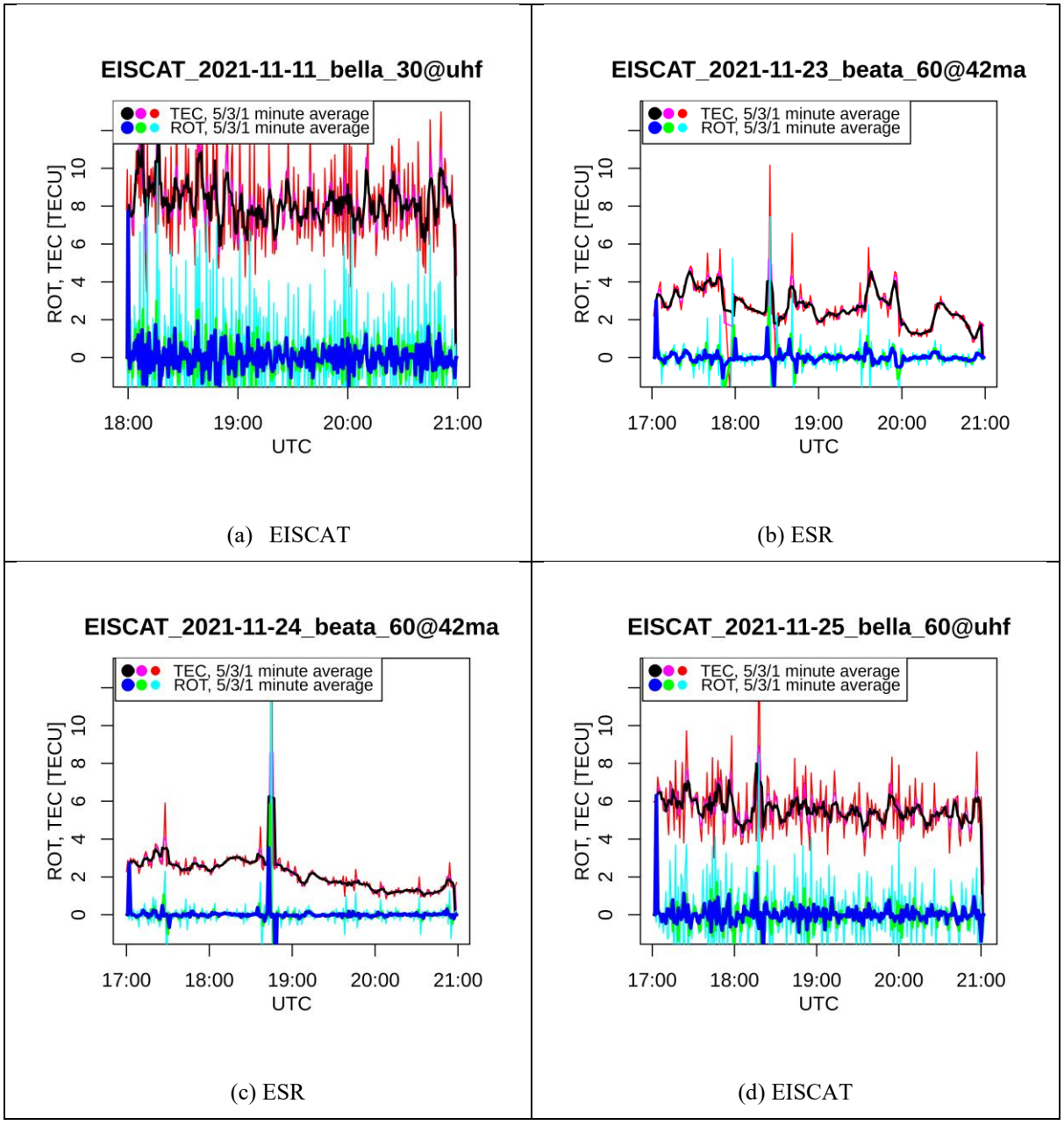

(a) EISCAT (b) ESR

(c) ESR (d) EISCAT

https://doi.org/10.5194/egusphere-2026-1741
Preprint. Discussion started: 1 June 2026

Figure 10: EISCAT/ESR TEC (in TECU) along the radars' beams in the case studies considered, obtained by integrating the electron density profiles. The radar ROT (in TECU min^{-1}) was obtained by differencing TEC values obtained over consecutive times. Initially, TEC and ROT were evaluated approximately every 60 s (red and cyan lines, respectively). However, in order to reduce the effect of noise (from the profiles estimates) the radar TEC was smoothed by using a 3-minute moving average (TEC in magenta and ROT in green) and by using a 5-minute moving average (TEC in black and ROT in blue).

The comparison between Fig. 7 and Fig. 10 suggests several aspects. The radar TEC appeared to be approximately constant although some slower changes (approximately of the order of one TECU across the observation interval) seemed to manifest at times in each day of the experiment. Some of the tenuous and slower trends in the radar TEC appeared to be plausible with trends observed in the 2D gaussian displacement parameter (compare, for example, Fig. 7(a) with Fig. 10(a)) although the evidence is at the limit of the combination of radar's sensitivity and noise.

https://doi.org/10.5194/egusphere-2026-1741
Preprint. Discussion started: 1 June 2026

3.3 GNSS

Figure 11 shows the ROT from several IGS GNSS ground stations in the area of EISCAT and KAIRA, with ray paths not aligned with EISCAT/KAIRA beams whilst traversing a common ionospheric volume.

600

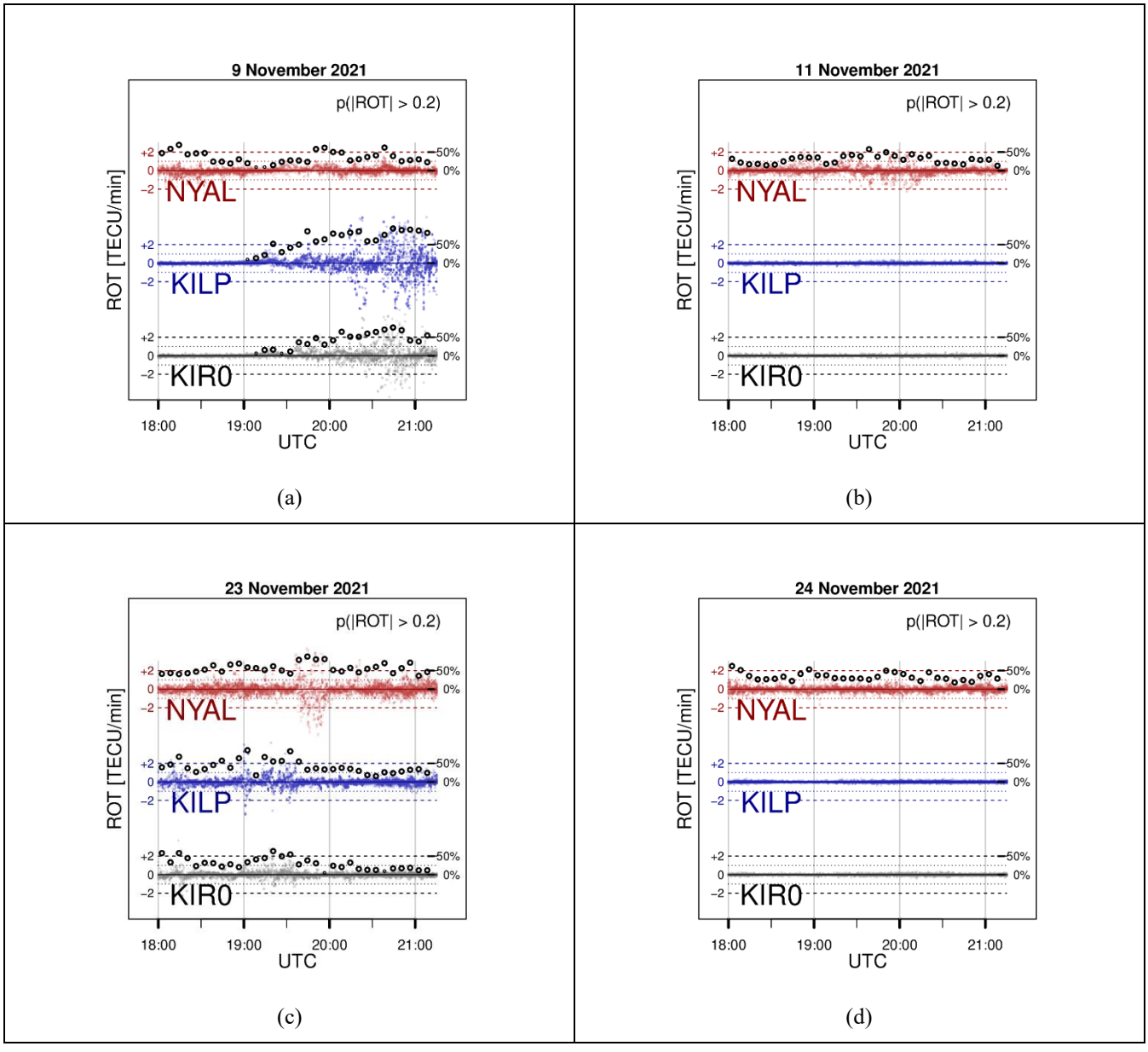

https://doi.org/10.5194/egusphere-2026-1741
Preprint. Discussion started: 1 June 2026

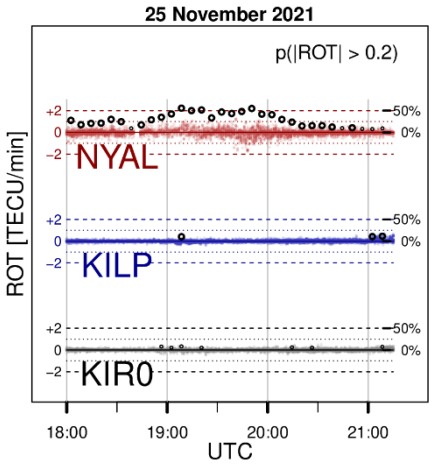

(e)

Figure 11: Rate of change of TEC (a measure of phase fluctuations on received radio signals) as observed by several IGS GNSS ground stations on the basis of L-band radio signals. Here, results from ground stations NYAL, KILP, and KIR0 are illustrated for 09 November 2021 18:00-21:00 UTC (a), 11 November 2021 18:00-21:00 UTC (b), 23 November 2021 18:00-21:00 UTC (c), 24 November 2021 18:00 - 21:00 UTC (d), and 25 November 2021 18:00-21:00 UTC (e).The probabilities that |ROT| values exceeded 0.2 TECU min^{-1} in any 3-minute interval are also indicated as black circles (circles in thicker lines represent probability values greater than 10%).

Figure 11 also shows the probability that |ROT| exceeds a given threshold (0.2 TECU min^{-1}). The probability p(|ROT| $\gtrsim$ 0.2 TECU min^{-1}) was calculated by dividing the number of all the GNSS observations showing |ROT| greater than the threshold by the number of all available GNSS 30 s observations in any 3-minute interval. Only GNSS satellites above an elevation angle of approximately $\approx 45°$ degrees were considered to limit observations within an ionospheric volume closer to both EISCAT/ESR and KAIRA fields of view. The background level of TEC fluctuations appears to be different between the three ground stations considered: NYA0 appears to show a generally higher background in ROT than the background at KIR0 and KILP. This is a consequence of ionospheric conditions generally different between the polar ionosphere (NYA0) and the auroral ionosphere (KIR0 and KILP), combined with different oscillators and logics implemented within these GNSS receivers. During quiet ionospheric conditions, GNSS |ROT| at KILP (almost co-located with KAIRA) appeared to be below a value approximately in the region of 0.2 TECU min^{-1}, hence considered as a "threshold" to distinguish ionospheric activity detected or undetected through GNSS. The ROT background during quiet ionospheric conditions at KIR0 appears to be somewhat higher than at KILP although in the region of approximately 0.2 TECU min^{-1}; it was higher than this threshold at NYA0 were conditions were generally more active throughout the experiment.

https://doi.org/10.5194/egusphere-2026-1741
Preprint. Discussion started: 1 June 2026

Phase fluctuations as quantified through ROT on GNSS signals showed enhancements above the given threshold only in limited time intervals throughout the observations. The main enhancement was observed on 23 November 2021 (and on 09 November 2021), whereas the occurrence of a sporadic E layer on 25 November 2021 (Fig. 9) did not correspond to any comparable enhancement in ROT.

From the results illustrated through Figs. 4 to 11 the following aspects can be deduced.

(1) The intensity fluctuations observed through KAIRA over its LBA and HBA generally seem to reflect the overall ionospheric conditions and structures detected through both EISCAT and ESR radars. Enhancements in intensity fluctuations seem more likely to occur in the presence of gradients observed in the EISCAT/ESR electron density profiles: higher levels of KAIRA VHF scintillation seemed to be associated even with tenuous ionisation gradients (as in the case of 25 November 2021). The magnitude of these fluctuations (as quantified through the S_4 intensity scintillation index) remained at low values suggesting an overall absence of multiple scattering, with irregularities thus localising around ionisation enhancements as detected through EISCAT/ESR electron density profiles.

(2) Enhancements in ROT as observed from ground GNSS stations (on the basis of L-band radio signals from different constellations) did not always correspond to an enhancement in KAIRA VHF intensity fluctuations. When compared with EISCAT/ESR electron density profiles, enhancements in ROT seemed to be caused by structured ionisation extending over a wider interval of altitudes rather than by ionisation gradients occurring across thinner layers (as in the case of a sporadic E layer starting to appear from about 20:00 UTC on 25 November 2021) (Forte et al., 2017).

(3) EISCAT and KAIRA measurements appeared to be located towards the equatorward edge of the auroral oval. Whilst a horizontal plasma drift appeared to be plausible given the presence of intensity fluctuations on KAIRA scintillation observations (low-confidence observations from the Tromsø dynasonde appeared to support this possibility), GNSS ROT observations did not seem to show a clear evidence for that.

(4) The source-zoomed image seemed to show some modifications during the more active ionospheric conditions. During less active conditions (as in the presence of a stable and tenuous layer on 11 November 2021), the centre brightness, the centre position, and the shape of the source image (as quantified through a 2D gaussian fit parameters) seemed to remain stable in the neighbourhood of their nominal values. However, during more active conditions (as in the case of 23 November 2021 and 25 November 2021), the source centre seemed to show time-varying levels of brightness, the source centre position seemed to show a time-varying displacement (with trends and fluctuations – summarised in Fig. 7), and the source shape seemed to show time-varying trends and fluctuations (please also refer to animations in supplementary material). Changes to the source-zoomed image (please refer to Fig. 7 and to animations in supplementary material) seemed also to occur in the presence of tenuous ionisation gradients (as in the case of 25 November 2021); these changes seemed consistent with KAIRA VHF scintillation measurements.

https://doi.org/10.5194/egusphere-2026-1741
Preprint. Discussion started: 1 June 2026

4. Discussion

The results of this experiment indicate the presence of geometry-dependent propagation effects such as phase fluctuations and intensity (or amplitude) scintillation. Whilst phase fluctuations arise from the propagation through electron density irregularities distributing over large-to-small spatial scales, intensity scintillation arises from small-scale irregularities characterised by spatial scales within the VHF inertial subrange of the electron density spatial fluctuations associated with the irregularities. These propagation effects were reflected in the observations carried out by means of three different instruments: gradients in the electron density distribution observed through EISCAT/ESR incoherent scatter radars, temporal phase and TEC fluctuations observed by means of ground GNSS receivers, intensity scintillation observed through KAIRA VHF beam-formed measurements. The propagation effects observed throughout the experiment also induced changes to the source-zoomed image which could be estimated from KAIRA all-sky images–simultaneously collected alongside beam-formed observations.

In relation to question (1) (i.e., what information can be deduced about ionospheric irregularities from the propagation effects observed in this experiment), the experiment indicated similarities as well as differences in the observations carried out by the three instruments.

Enhancements in temporal TEC fluctuations ($|\mathrm{ROT}| \gtrsim 0.2$ TECU min^{-1}) detected by means of ground GNSS receivers corresponded to enhancements in KAIRA VHF scintillation on 23 November 2021. Although technical problems prevented from accessing usable EISCAT observations on this day, it is plausible to assume (by using evidence from ESR observations on 23 November 2021 as well as from EISCAT/ESR on 09 November 2021, in conjunction with evidence from corresponding GNSS ROT observations) that irregularities formed and distributed over a wider interval of altitudes (between the E and F regions), over larger spatial horizontal scales, and were characterised by marked gradients in the electron density. These aspects were enough to induce phase fluctuations and, therefore, enhancements in TEC fluctuations, as observed through L-band GNSS radio signals (Forte et al., 2013; Forte et al., 2017; John et al., 2021a; John et al., 2021b).

The situation was different on 11 November 2021 and 24 November 2021 with low KAIRA VHF scintillation and no enhancements in TEC fluctuations (from GNSS ground stations KIR0 and KILP in the proximity of EISCAT and KAIRA). There was tenuous ionisation at F-region altitudes (as indicated by EISCAT electron density profiles): the ionisation gradients associated with this feature were not intense enough to induce an enhancement in phase fluctuations, GNSS TEC fluctuations ($|\mathrm{ROT}| \lesssim 0.2$ TECU min^{-1}), and KAIRA VHF scintillation (Forte et al., 2013; Forte et al., 2017; John et al., 2021a; John et al., 2021b).

On the other hand, the situation on 25 November 2021 was quite intriguing. Here, a tenuous ionisation layer could be observed to form in the F region about 18:00 UTC, with gaps in ionisation just about noticeable around approximately 18:15 UTC and

https://doi.org/10.5194/egusphere-2026-1741
Preprint. Discussion started: 1 June 2026

approximately between 19:15 UTC and 20:00 UTC. In this case, enhancements in KAIRA VHF intensity scintillation were observed in conjunction with these gaps in ionisation although no clear enhancements in TEC fluctuations could be detected from ground GNSS receivers. The evidence in this case suggests that the ionisation gradient was not extended enough in altitude and not intense enough to induce a signature on GNSS signals: however, the gaps in ionisation detected through EISCAT suggest the presence of patchy irregularities. Generally, in order to induce intensity scintillation, irregularities need to form in the inertial subrange of the electron density spatial fluctuations and need to drift across the ray path: the inertial subrange for ionospheric irregularities is approximately of the order of up to few kilometres at VHF. Considering that the spatial resolution of EISCAT electron density profiles is approximately of the order of tens of kilometres at F region altitudes, it is plausible to conclude that irregularities capable of inducing VHF scintillation were present in the F region on 25 November 2021 (between approximately 18:30 UTC and 20:00 UTC) with spatial scales in the inertial subrange: however, these spatial scales appeared to be smaller than the radar resolution.

Interestingly, a sporadic E layer could be observed to form from about 20:00 UTC on 25 November 2021, with electron density values intensifying closer to/after 21:00 UTC (the end of the experiment), whilst generally decreasing in the F region. This feature corresponded with some enhancements in GNSS temporal TEC fluctuations at the station in KILP (more pronounced than at KIR0), though overall smaller in magnitude in comparison with TEC fluctuations associated with more intense structures extending between the E and F region altitudes (e.g., during 23 November 2021). These differences suggest a spatially patchy nature of the sporadic E layer detected by EISCAT. In turn, the VHF intensity fluctuations observed through KAIRA between 20:00 UTC and 21:00 UTC were smaller than between 18:30 UTC and 20:00 UTC (the scintillation index was also very low). The lack of more pronounced enhancements in VHF scintillation suggests that the irregularities associated with this sporadic E layer did not have gradients in the inertial subrange intense enough to induce scintillation and that they were probably forming over spatial scales larger than those in the inertial subrange. Considering that the spatial resolution of EISCAT electron density profiles is approximately of the order of few kilometres at E region altitudes, it is plausible to conclude that this type of irregularities (with spatial scales between approximately few kilometres and few tens of kilometres) can be detected through EISCAT, can induce small phase fluctuations on GNSS signals, but are less capable of inducing scintillation at VHF.

Information about the plasma drift can be deduced from KAIRA VHF 1D power spectra for zero-mean normalised intensity fluctuations. These spectra indicate a power-law after a Fresnel frequency of the order of approximately between 0.02 Hz and 0.06 Hz (please refer to Fig. A1 and discussions in Appendix A) in the case of lower intensity fluctuations (i.e., 11 November 2021, 24 November 2021, and 25 November 2021). In these cases, weak scattering can be a good approximation where smaller intensity fluctuations are assumed to arise from the propagation through a phase-changing screen at a given distance from the receiving point. In the weak scattering approximation, the concept of the Fresnel frequency can be invoked to relate the horizontal plasma drift (in the phase-changing screen) with the distance to the phase-changing screen (more details are provided

https://doi.org/10.5194/egusphere-2026-1741
Preprint. Discussion started: 1 June 2026

in Appendix A). Within this approximation, a plasma drift approximately of the order of few tens of $\mathrm{m} \cdot \mathrm{s}^{-1}$ appears to be plausible for irregularities (and a phase screen) between the E and F regions in the ionosphere.

In the presence of a horizontal plasma drift (as suggested by the Tromsø dynasonde observations as well as by the presence of intensity fluctuations on KAIRA beam-formed VHF observations – more details can be found in Appendix A) the propagation through ionisation structures induces temporal fluctuations in the intensity and phase of the received radio waves only if the spatial gradients in the inertial subrange associated with these structures are intense enough to cause a detectable deformation of the wavefront. Hence, even in the presence of a plasma drift across the ray paths the sensitivity of different instruments relies on the detectability of propagation disturbances, which depends on the combination between wavelength, spatial ionisation gradients, propagation geometry, and the architecture of the receiver utilised (i.e., whether a satellite radio receiver or an interferometer): this aspect needs careful consideration when utilising diverse observations.

An important aspect in the comparison of phase fluctuations and intensity scintillation between observations from artificial satellites and those from astrophysical sources of radio waves is the angular size of the source. In the former case, the assumption that the satellite transmitter behaves as a point-like source seems to be a good approximation in the treatment of the propagation problem. However, astrophysical sources are extended and introduce a spatial filtering effect (Hewish et al., 1964; Little and Hewish, 1966; Budden and Uscinski, 1970; Ishimaru, 1978; Manoharan and Ananthakrishnan 1990; Yamauchi et al. 1996) with the net result of reducing the magnitude of intensity fluctuations observed, for example, in the presence of scintillation (Ishimaru, 1978). For an ionospheric height of approximately of the order of $200 - 300$ km, the critical size for ionospheric scintillation over the LBA frequency range is approximately of the order of 5-10 arcminutes (Narayan, 1992; Chhetri et al., 2018). de Gasperin et al. (2020) show that at these frequencies, whilst some of the flux density of Cas A is more concentrated, most of it is spread over a circle 5 arcminutes in diameter. Therefore, provided observations are in the weak scattering regime, the effects due to a finite source size are likely to be minor in the LBA band, but increasingly important across the HBA band.

Furthermore, the observation of astrophysical radio sources can be still affected by propagation effects introduced somewhere else along the ray path, which need to be assessed as well (Forte et al., 2022). In the case of the experiment presented here, the KAIRA observations were in the local nighttime, hence pointing away from the Sun. In the days considered for this experiment, OMNI observations (available at https://omniweb.gsfc.nasa.gov/form/dx1.html) seemed to indicate constant conditions in terms of electron density and plasma velocity in the heliosphere (apart from enhancements visible earlier on the day 11 November 2021) (Papitashvili and King, 2020). The evidence from OMNI combined with the fact that, in general, Cas A is very extended makes it very unlikely that there would be any signature from the heliosphere: the source needs indeed to be compact on arcsecond scales, hence more than two orders of magnitude smaller than for ionospheric scintillation. Also, the

https://doi.org/10.5194/egusphere-2026-1741
Preprint. Discussion started: 1 June 2026

Fresnel frequencies observed in the KAIRA scintillation measurements (please refer to Fig. A1 and discussions in Appendix A) appeared to be plausible with the inertial subrange of irregularities and plasma drift developing at ionospheric altitudes.

Therefore, in relation to question (1), the experiment revealed that in the presence of more intense ionisation gradients forming over an extended interval of altitudes between the E and F regions, phase fluctuations and scintillation can be observed through GNSS and KAIRA VHF, respectively. However, in the presence of more tenuous ionisation gradients forming over a reduced interval of altitudes and over smaller spatial scales, KAIRA VHF observations appear to have a higher sensitivity than GNSS in detecting propagation effects induced by this type of ionisation gradients. In the latter case, measurements such as those carried out through KAIRA VHF beam-formed scintillation and EISCAT, reveal the existence of ionisation structures which are undetected when utilising GNSS alone, even in the presence of a horizontal plasma drift across the ray paths. This is due to the dispersive nature of the ionosphere as well as to the increase in phase fluctuations and scintillation with decreasing radio wave frequency: this aspect was demonstrated already by means of earlier LEO satellite observations over multiple frequencies (Fremouw et al., 1978; Forte, 2008). However, contrary to satellite observations, scintillation measurements such as those provided through KAIRA VHF beam-forming offer a new way to detect the presence of ionisation structures because they allow to disentangle spatial and temporal variability given that the radio source position varies more slowly than a LEO satellite source.

When utilised in conjunction with traditional ionospheric instruments (e.g., GNSS, EISCAT) these new observations demonstrate the multiple spatial scales over which irregularities form and evolve in the ionosphere, hence providing more evidence on instability and formation mechanisms. The combination of the higher sensitivity offered by instruments such as KAIRA (or LOFAR, MWA, and similar) with traditional ionospheric instruments is essential to improve the current understanding of ionospheric physics and to advance the modelling of the overall response of the magnetosphere-ionosphere system to adverse space weather conditions.

In relation to question (2) (i.e., how ionospheric propagation disturbances affecting all-sky images, collected through KAIRA or other similar instruments - such as LOFAR, MWA, SKA-Low - can be utilised to deduce information about ionospheric structures and processes), the experiment simultaneously collected KAIRA VHF scintillation observations (beam-formed estimates of radio waves intensities received from Cas A) and KAIRA all-sky images (visibility function for the field of view). Although the sensitivity and the field of view of the KAIRA station are lower than those of a standard LOFAR station, this experiment still enabled focussing on low-resolution images of the source Cas A (a portion of the all-sky image, as detailed in section 2.1.3).

Propagation disturbances originating in the ionosphere appeared to affect the image of a source by means of two concurring aspects: slower trends and faster changes (or fluctuations). The faster changes in the source parameters (D, σ_x, and σ_y) can be

https://doi.org/10.5194/egusphere-2026-1741
Preprint. Discussion started: 1 June 2026

explained with degradations in the goodness of the 2D gaussian fit. Instances of weaker fits can be due to enhancements in scintillation where noise and other parts of the source-zoomed image may have higher contributions (the resulting effect on the source image is similar to optical blurring): these instances affect both the source centre displacement and the fit standard deviations. In the presence of enhancements in scintillation (as observed through KAIRA beam-formed measurements), the amplitude of the source brightness is reduced due to scattering: in this case, the 2D gaussian fit locks onto other structures present in the area of the fit. Nonetheless, the relative magnitudes of slower trends and faster changes in the source centre displacement D appear to be roughly in line with the predictions of Waszewski et al. (2022), who derived an expected relationship between the magnitude of refractive shifts in the presence of scintillation and the scintillation index. The diameter of KAIRA is smaller compared with the Fresnel scale at the radio wave frequencies considered here: this aspect limits the sensitivity of the fitted σ_x, and σ_y to effects induced by irregularities with spatial scales in the inertial subrange. Under this framework, here the source centre displacement D provides a robust first-order proxy for refractive variability, whereas σ_x, and σ_y are informative when the fit remains source-dominated and the gaussian fit remains a reasonable local approximation. Nevertheless, this approach can be generalised to larger and future arrays, with higher sensitivity for the fitted σ_x, and σ_y. The presence of a stronger background around the source can also lead to an underestimate of the S_4 index from beam-formed observations: hence, limiting the sensitivity to small-scale irregularities in the inertial subrange.

On the other hand, the slower trends in the source parameters, particularly the source centre displacement D can be explained with the presence of ionisation gradients (which are probably approximately $\ll 0.2$ TECU min^{-1}) drifting across the instrument field of view: instruments such as EISCAT and GNSS can only detect ionisation gradients that are larger than their resolution limit (i.e., intense enough and extended over a range of altitudes capable of producing a signature that can be appreciated by the two instruments). Incidentally, these slower trends in the source centre displacement D cannot be explained merely through an elevation angle effect as they appear to be inconsistent with the decrease in elevation angle throughout the experiment.

The spectra for the source centre displacement D (please refer to Fig. A3 and discussions in Appendix A) indicate temporal changes that can be plausible with tenuous plasma gradients occurring between the E and F regions of the ionosphere and traversing the array's aperture as a consequence of horizontal plasma drift and/or localised ionisation mechanisms. Whilst the ionospheric origin of these ionisation gradients occurring over the KAIRA's field of view appeared to be plausible (please refer to discussions in Appendix A), the resolution and sensitivity of the current EISCAT radar and of typical GNSS ionospheric observations appeared to be not always sufficient to detect these ionospheric gradients.

In general, KAIRA VHF observations (beam-formed and all-sky images) seemed to indicate also the presence of ionisation structures which were not readily detectable by means of typical ionospheric instruments like EISCAT/ESR and GNSS (or

https://doi.org/10.5194/egusphere-2026-1741
Preprint. Discussion started: 1 June 2026

even completely absent in their measurements). It is important to notice that the observations carried out through KAIRA indicated spectral features (please see discussions in Appendix A) which appeared to be plausible with irregularities originating in the ionosphere. Although single-station observations can be ambiguous (Forte et al., 2022), the enhancement in fluctuations in the function $\beta(t)$ appears to be consistent with the overall ionospheric state in the auroral/polar region where the measurements were carried out, as assessed by means of EISCAT/ESR and GNSS. However, KAIRA observations seemed to reveal higher sensitivity to weaker ionisation structures which may not be detected by EISCAT/ESR and GNSS: the electron density gradients associated with these weaker ionisation structures appeared to be not intense enough and not extended enough in altitude to induce a signature on GNSS signals and/or to be detectable within EISCAT/ESR spatial resolution (increasing from few kilometres in the E region to tens of kilometres in the F region). Whilst the spatial separation between EISCAT and KAIRA's fields of view seems to be an aspect to consider in the differences between electron density profiles and beam-formed VHF scintillation, the all-sky images reflect the overall ionospheric state in the common ionospheric volume sampled by the three instruments.

Observations such as those produced by KAIRA (and, similarly, by instruments such as LOFAR, MWA, SKA-Low) for all-sky and source-zoomed images provide a new way to detect ionisation structures which may be not readily detectable through other traditional ionospheric instruments. Contrary to traditional satellite experiments over few radio wave frequencies, this type of observations allows to uncover new ionospheric physics which is essential for a comprehensive description of mechanisms taking place in the ionosphere and necessary for accurate predictions of the ionospheric state in the presence of given space weather conditions. Incidentally, an attempt to calibrate low-frequency radio astronomy observations by using GNSS TEC maps (and, perhaps, ROTI maps) might not be able to capture these effects given a higher sensitivity in radio telescope observations as compared with TEC and ROTI maps deduced from a network of ground GNSS receivers.

The situation explored within this experiment can be summarised by the sketches in Fig. 12. At observation point A an enhancement in KAIRA (or instruments such as LOFAR, MWA, SKA-Low) VHF scintillation and in GNSS ROT can be observed. However, at observation point B an enhancement in KAIRA (or instruments such as LOFAR, MWA, SKA-Low) VHF scintillation does not correspond to any enhancement in GNSS ROT (Forte et al., 2023a; Forte et al., 2023b).

https://doi.org/10.5194/egusphere-2026-1741
Preprint. Discussion started: 1 June 2026

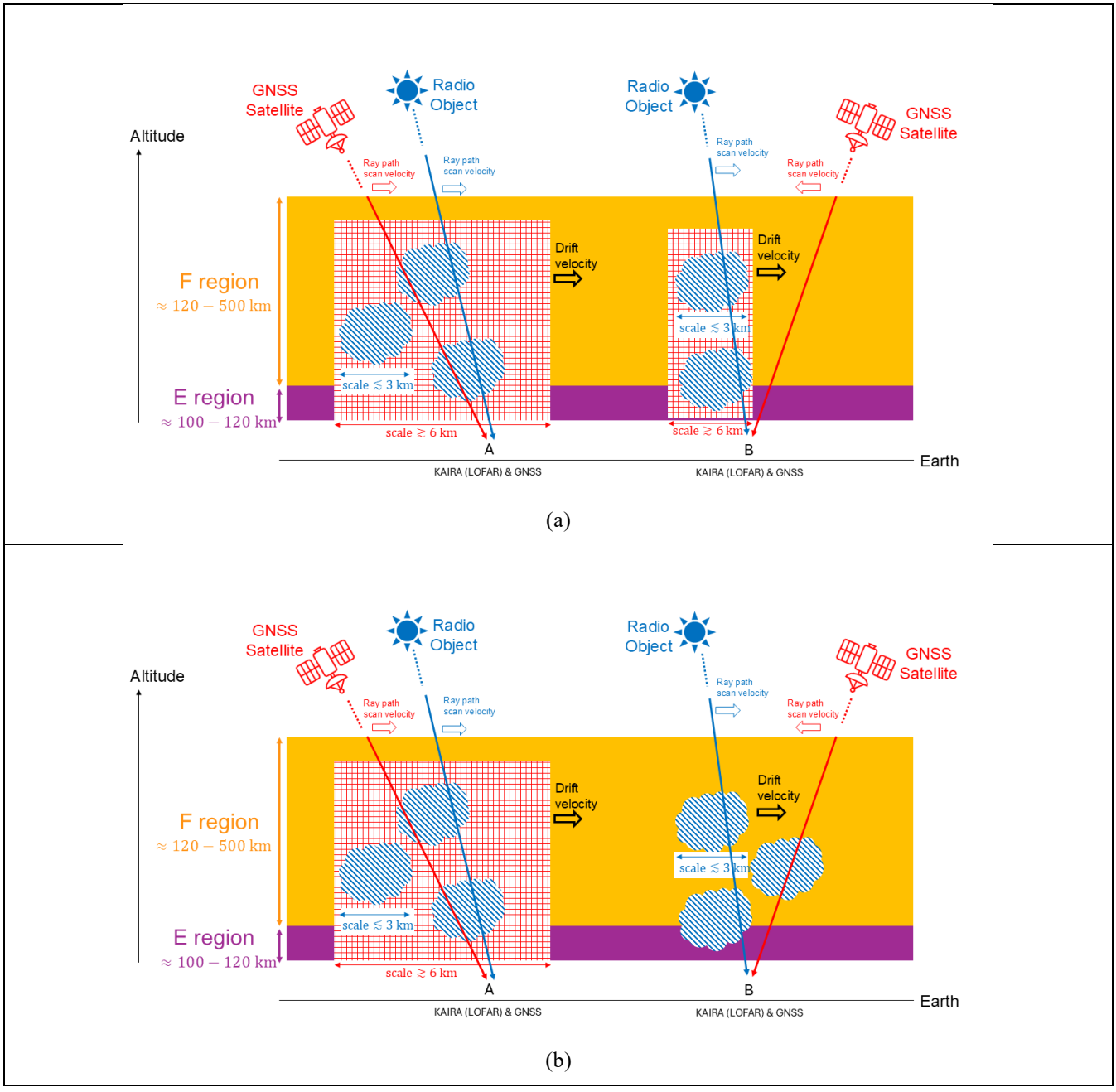

Figure 12: An illustration of the sensitivity of KAIRA (or instruments such as LOFAR, MWA, SKA-Low) and GNSS observations in relation to ionospheric structures (Forte et al., 2023a; Forte et al., 2023b). The illustration indicate how different instruments might return either apparently similar - or different - observations, depending on the scenario. At point A, an enhancement in KAIRA (or similar to LOFAR) VHF scintillation and in GNSS ROT can be observed, due to irregularities

https://doi.org/10.5194/egusphere-2026-1741
Preprint. Discussion started: 1 June 2026

distributing over large-to-small spatial scales. At point B an enhancement in KAIRA (or similar to LOFAR) VHF scintillation does not correspond to any enhancement in GNSS ROT, due to the presence of small scale irregularities only (no irregularities with larger spatial scales).

https://doi.org/10.5194/egusphere-2026-1741
Preprint. Discussion started: 1 June 2026

5. Conclusions

A multi-instrument experiment to explore radio propagation effects on a range of radio wave frequencies was conducted in the European auroral and polar sectors in November 2021. This experiment (the first of its kind) collected simultaneous observations of radio wave scintillation occurring on signals emitted from Cas A (by means of KAIRA beam-formed VHF scintillation measurements), observations of electron density profiles along the Cas A line of sight (by means of EISCAT incoherent scatter radars), observations of propagation effects quantified through the rate of change of TEC (ROT) on GNSS signals (by means of ground GNSS receivers in the surrounding of KAIRA and EISCAT/ESR), observations of all-sky and Cas A-zoomed images (by means of KAIRA all-sky imaging). This experiment demonstrated how evidence from diverse instruments and datasets can be combined to extract new information about the ionosphere and its spatio-temporal evolution.

The impact and the origin of propagation effects on the image of the source Cas A were characterised on the basis of a novel approach which fitted a 2D gaussian function to a pixelated version of the source-zoomed image (a portion of the all-sky visibility image around Cas A) as well as through the combination of evidence from GNSS, EISCAT/ESR, and KAIRA beam-formed observations.

For the first time, the experiment demonstrated that more intense and extended (in altitude) ionisation gradients ($|\mathrm{ROT}| \gtrsim 0.2$ TECU min^{-1}) originating in the ionosphere can be detected by means of EISCAT (electron density profiles) and induce propagation disturbances detectable through GNSS (phase fluctuations) and KAIRA (VHF scintillation). However, more tenuous and/or narrower ionisation gradients amounting to $|\mathrm{ROT}| \lesssim 0.2$ TECU min^{-1} and capable of inducing VHF scintillation can be detected by means of KAIRA but not necessarily through GNSS and EISCAT (due to not enough sensitivity and resolution). These propagation disturbances originating in the ionosphere can induce modifications to the position and shape of astronomical sources (such as those observed in radio astronomy) by means of two concurring aspects: slower trends (in the case of this experiment, associated with changes in the ionisation probably $\ll 0.2$ TECU min^{-1} and occurring across the array due to horizontal plasma drift and/or local ionospheric mechanisms) and degradations in the estimates of source position and shape (arising from enhancements in scintillation, when noise and other parts of the sky around a given source have higher contributions – an effect similar to optical blurring).

The combination of observations from these diverse instruments and datasets in a coordinated experiment provided conclusive evidence that ionisation gradients in the ionosphere can occur over various (or multiple) spatial scales. Ionospheric irregularities with spatial scales within the VHF inertial subrange (smaller than approximately few kilometres) and with weaker ionisation gradients can induce scintillation on radio waves from specific radio sources but *cannot* be detected through traditional ionospheric observations such as from EISCAT or GNSS. Irregularities in the VHF inertial subrange can occur in conjunction with larger spatial scales or in isolation as a consequence of local instability mechanisms. Their presence can be

https://doi.org/10.5194/egusphere-2026-1741
Preprint. Discussion started: 1 June 2026

detected through the combination of observations from different instruments (e.g., EISCAT, GNSS, ionosondes, radio telescopes).

The higher sensitivity offered by modern radio telescopes offers a new way to detect and characterise the spatial and temporal evolution of these ionisation gradients that appears to be superior to traditional satellite observations. However, it is the combination of observations from modern radio telescopes with observations from traditional ionospheric instruments (rather than the use of stand-alone radio telescopes) that enables novel understanding of ionospheric physics as well as a more accurate modelling of the ionospheric response to various space weather conditions over multiple spatial scales.

https://doi.org/10.5194/egusphere-2026-1741
Preprint. Discussion started: 1 June 2026

Appendix A

In the presence of weak scattering, the low intensity scintillation arising from the propagation through plasma density irregularities can be approximated with the concept of a phase-changing screen, where these irregularities are assumed to be confined and distributed within. If the irregularities within the phase screen drift across the ray path, it can be shown that fluctuations in the spatial plasma density distribution originate temporal fluctuations in the intensity of radio waves received after traversing the phase screen (Ishimaru, 1978; Forte et al., 2022). In this case, the 1D power spectral density $\Phi_I(\nu)$ for the intensity fluctuations of the received radio wave tend to exhibit an asymptotic power law for $\nu > \nu_F$ and an asymptotically constant behaviour for $\nu < \nu_F$. The parameter ν_F corresponds to the Fresnel frequency and it is given by:

$$\nu_F = \frac{V^{REL}}{\sqrt{2\lambda z_R}} \qquad (A1)$$

where V^{REL} is the drift velocity of plasma irregularities relative to the ray path, λ is the wavelength, and z_R indicates the distance between the receiving point and the phase screen.

The 1D power spectral densities $\Phi_I(\nu)$ for the zero-mean normalised intensity fluctuations observed through KAIRA beam-formed scintillation measurements are illustrated in Fig. A1 for the various days under consideration. The normalisation was based on the estimate of a moving mean average over 5 minutes (function *movmean* in MATLAB): in this case, 5 minutes were considered here as a comparison with the 3-minute detrending (utilised in Fig. 5-6). The spectra in Figure A1 were calculated every 5 minutes intervals. A power-law behaviour can be observed on 11, 24, and 25 November 2021, whereas on 23 November 2021 spectral modifications can be observed in correspondence of higher scintillation where multiple scattering needs to be taken into account rather than a description based on a single phase-changing screen (Forte, 2008).

https://doi.org/10.5194/egusphere-2026-1741
Preprint. Discussion started: 1 June 2026

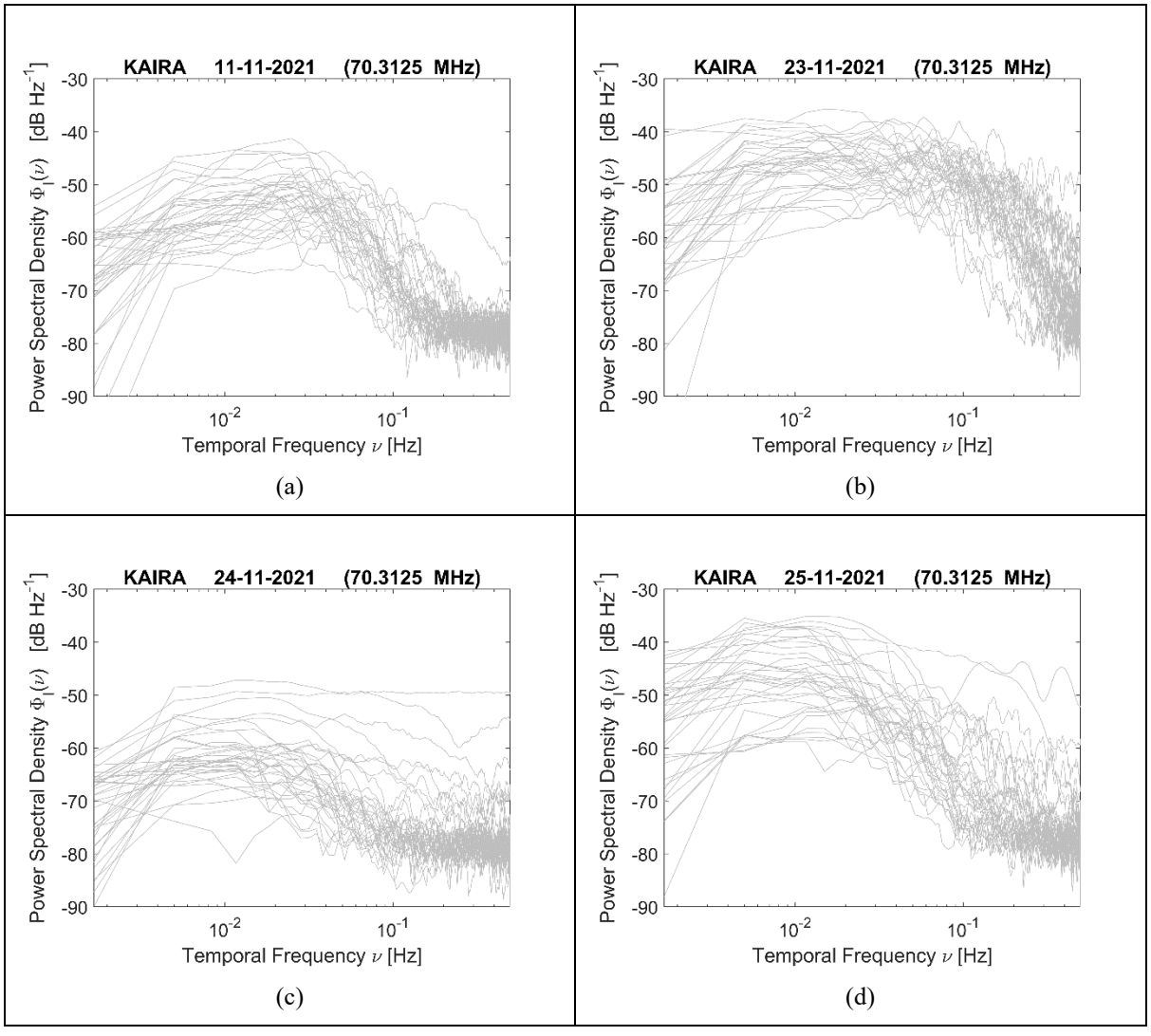

935 **Figure A1:** 1D power spectral density $\Phi_I(\nu)$ for the zero-mean, normalised, beam-formed intensity fluctuations for a radio wave frequency of approximately 70.3 MHz (similar to the frequency at which all-sky images were collected). Every grey line corresponds to an estimate of $\Phi_I(\nu)$ over a 5-minute time interval.

Under the assumption of weak scattering, it is possible to utilise the concept of the Fresnel frequency in Eq. (A1) to infer 940 possible values for the plasma drift as well as for the distance to the screen. Figure A2 illustrates the possible combinations of V^{REL} and z_R values corresponding to different values of the Fresnel frequency according to the evidence from Fig. A1 (a, c, d).

https://doi.org/10.5194/egusphere-2026-1741
Preprint. Discussion started: 1 June 2026

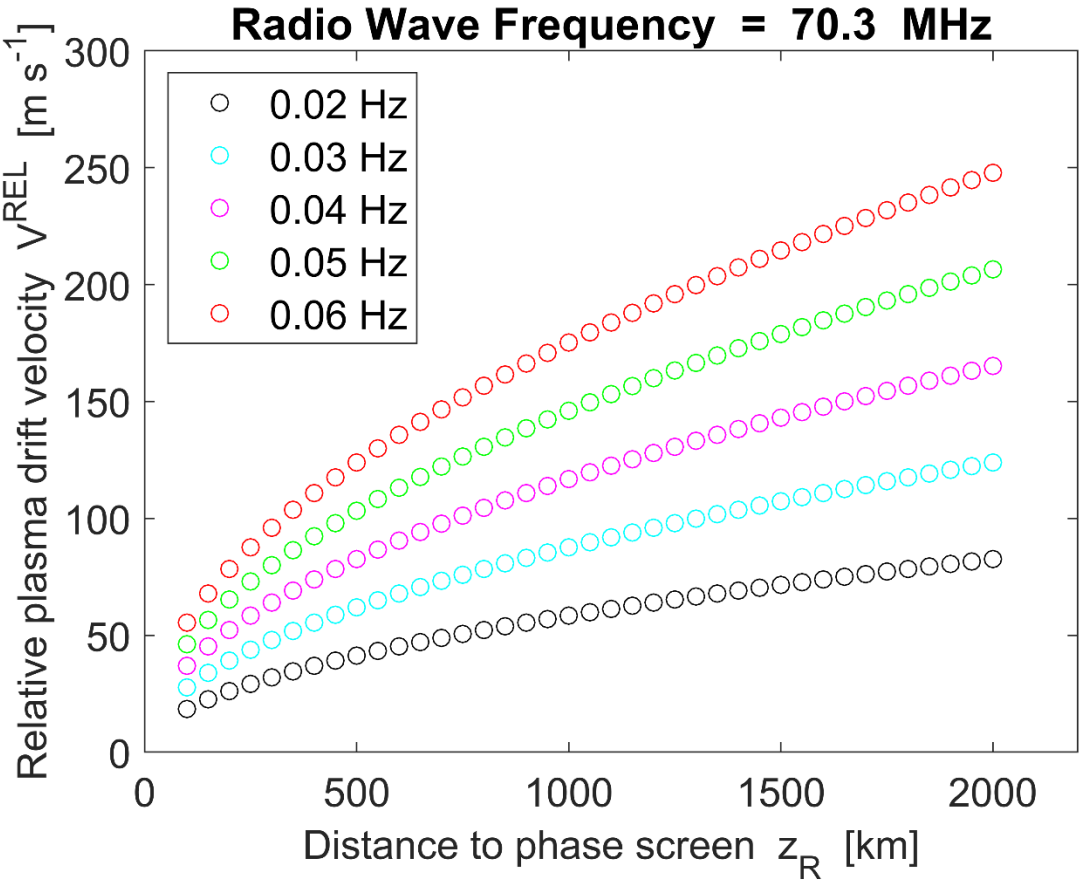

945

Figure A2: Different values for the distance to the phase screen and the relative plasma drift velocity corresponding to different values of the Fresnel frequency (e.g., between 0.02 Hz and 0.06 Hz, as shown in Fig. A1), based on Eq. (A1).

From Fig. A2 a higher plasma drift velocity appears to be consistent with a phase screen in the topside ionosphere (or, further
950 into the plasmasphere), whereas a lower plasma drift velocity appears to be consistent with a phase screen in the E or F regions (or both). Irregularities at higher altitudes or larger distances z_R (e.g., in the plasmasphere or in the heliosphere) would require a drift velocity V^{REL} generally higher than in the ionosphere in order to be consistent with the observed Fresnel frequencies (Forte et al., 2022).

955 On the other hand, the temporal fluctuations observed in the source displacement D, estimated through a 2D gaussian fit on the pixelated source-zoomed image, appear to exhibit a behaviour somehow similar to $\Phi_I(\nu)$ (Fig. A3). Figure A3 shows the power spectral density for the displacement D, $\Phi_D(\nu)$, estimated every 5 minutes (grey lines) though without any detrending. In Fig. A3 slower changes are responsible for spectral components at lower frequencies ($\lesssim 10^{-2}$ Hz) whereas the faster

https://doi.org/10.5194/egusphere-2026-1741
Preprint. Discussion started: 1 June 2026

fluctuations appear to be in an interval of spectral frequencies similar to $\Phi_I(\nu)$ (trends were removed from the zero-mean normalised intensity).

Given the evidence from Fig. A2 and from Fig. A3, it is plausible to conclude that the changes to the source shape and position appeared to be likely originated in the ionosphere due to two possible concurring aspects: slower trends were probably induced by changes in the ionospheric plasma density across the array's field whereas degradations appearing as faster changes were likely due to scintillation. The slower trends can be explained with weaker ionisation gradients traversing KAIRA's field of view under the effect of horizontal plasma drift and/or local ionisation mechanisms in the ionosphere. On the other hand, the faster changes can be associated with degradations in the gaussian fit in the presence of scintillation, when noise and other parts of the source-zoomed image may become prevalent (this effect is similar to optical blurring).

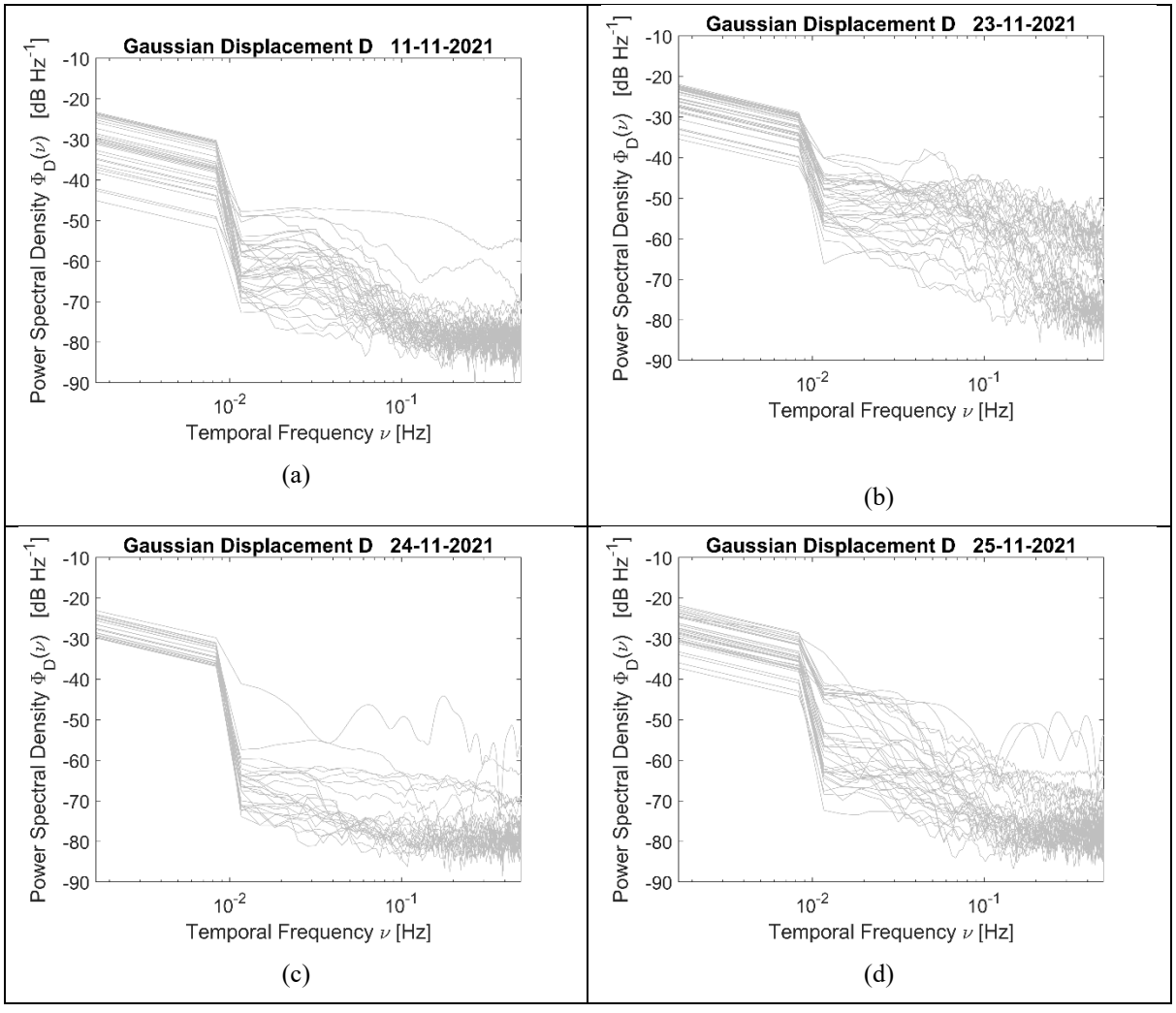

https://doi.org/10.5194/egusphere-2026-1741
Preprint. Discussion started: 1 June 2026

Figure A3: 1D power spectral density $\Phi_D(\nu)$ for the gaussian-fitted displacement of the source centre. In this case no detrending and no zero-mean were applied. The faster changes are attributable to degradations in the goodness of the 2D gaussian fit on the pixelated source-zoomed image). Every grey line corresponds to an estimate of $\Phi_D(\nu)$ over a 5-minute time interval.

Authors' contribution

Conceptualisation: Forte. **Experiment supervision:** Forte, Krankowski, Häggström, Fallows. **Experiment running:** Häggström, Fallows, McKay, Kero. **Data contribution:** Häggström, McKay, Kero. **Methodology:** Forte, Krankowski, Flisek, Kotulak, Morgan, Błaszkiewicz, McKay. **Analysis:** Forte, Flisek, Kotulak, Morgan, Błaszkiewicz, McKay, Kinsler, Lu, Fron, Kownacki, Radzanowski, Bisi. **Discussion:** All Authors. **Writing (original draft):** Forte. **Writing (review and editing):** Forte, Bisi, Krankowski, Kotulak, Flisek, Morgan, McKay, Lu, Kinsler, Błaszkiewicz, with contributions and approval from all Authors. **Funding:** Forte, Bisi, Krankowski, Fallows, Häggström, Kero.

Competing interests

The Authors do not have any competing interests.

Data Availability

KAIRA: KAIRA was funded by the University of Oulu and the FP7 European Regional Development Fund and is operated by the Sodankylä Geophysical Observatory/University of Oulu, Finland. KAIRA data availability is handled according to the SGO's data licence (https://www.sgo.fi/Data/licence.php) and the dataset used here can be made available as required by the publication.

EISCAT: EISCAT is an international association supported by research organizations in China (CRIRP), Finland (SA), Japan (NIPR and STEL), Norway (NFR), Sweden (VR), and the United Kingdom (NERC). EISCAT/ESR data are available at http://portal.eiscat.se/schedule/schedule.cgi.

GNSS: RINEX data were accessed through the International GNSS Service (IGS) (https://cddis.nasa.gov/archive/gnss/products/) (Noll, 2010; Johnston et al., 2017).

https://doi.org/10.5194/egusphere-2026-1741
Preprint. Discussion started: 1 June 2026

The animations for all-sky images are available in supplementary material accessible at https://zenodo.org/records/18986049?preview=1&token=eyJhbGciOiJIUzUxMiJ9.eyJpZCI6ImVmOTMxN2MyLWFiYjUtNGQ1MC1iNjRhLWFjZDg2YzM1MTgxYSIsImRhdGEiOnt9LCJyYW5kb20iOiIwMmViMzcyNGJkNGYwMDkzNzNkYjUzZTEwNGEwYzlhOSJ9.Zbkj9LyU4eE_u_qUmoNMiuK4gtR_Y8cVmf7B2VZMdiYNBfl3ZrGFEYbvG_-sxjrPTBbWFNxN8UuyH0dTDazt8A).

https://doi.org/10.5194/egusphere-2026-1741
Preprint. Discussion started: 1 June 2026

Acknowledgments

KAIRA was funded by the University of Oulu and the FP7 European Regional Development Fund and is operated by the Sodankylä Geophysical Observatory/University of Oulu, Finland..

EISCAT is an international association supported by research organizations in China (CRIRP), Finland (SA), Japan (NIPR and STEL), Norway (NFR), Sweden (VR), and the United Kingdom (NERC). EISCAT/ESR data are available at http://portal.eiscat.se/schedule/schedule.cgi.

The EISCAT campaigns were supported through the EISCAT UK time allocation (funded through the UK Natural Environment Research Council).

The work at the University of Bath was supported by the UK Natural Environment Research Council (NERC) [grant numbers NE/R009082/1, NE/V002597/1, NE/W003074/1, NE/X019004/1].

A.K., K.K., L.B., P.F., A.F., M.K. and B.R. acknowledge the Ministry of Science and Higher Education of Poland for granting funds for the Polish contribution to the LOFAR ERIC, LOFAR2.0 upgrade (decision number: 2021/WK/2) and for maintenance of the LOFAR PL-612 Bałdy station (decision number: 28/530020/SPUB/SP/2022) and Lamkowko Satellite Observatory (decision number: 22/566625/SPUB/SP/2023).

The authors acknowledge the use of NASA/GSFC's Space Physics Data Facility's OMNIWeb service, and OMNI data.

The authors are very grateful to Dr Maaijke Mevius for helpful discussions regarding this work.

https://doi.org/10.5194/egusphere-2026-1741
Preprint. Discussion started: 1 June 2026

References

Aarons J. (1997). Global Positioning System Phase Fluctuations at Auroral Latitudes, Journal of Geophysical Research, Vol. 102, N. A8, pp. 17219–17231, https://doi.org/10.1029/97JA01118.

Bisoi S. K., Janardhan P., Ingale M., Subramanian P., Ananthakrishnan S., Tokumaru M. and Fujiki K. (2014). A study of density modulation index in the inner heliospheric solar wind during solar cycle 23. The Astrophysical Journal, 795(1), p.69, doi:10.1088/0004-637X/795/1/69.

Booker H. G. and Majidiahi G. (1981). Theory of refractive scattering in scintillation phenomena. Journal of Atmospheric and Terrestrial Physics, 43(11), 1199-1214, https://doi.org/10.1016/0021-9169(81)90035-0.

Briggs, B. H., and Parkin, I. A. (1963), On the variation of radio star and satellite scintillations with zenith angle, Journal of Atmospheric and Terrestrial Physics, 25(6), 339-366, https://doi.org/10.1016/0021-9169(63)90150-8.

Budden K. G., and Uscinski B. J. (1970). The scintillation of extended radio sources when the receiver has a finite bandwidth, Proceedings of the Royal Society of London. A. Mathematical and Physical Sciences, Vol. 316, Issue 1526, pp. 315-339, https://doi.org/10.1098/rspa.1970.0082.

Calabretta, M. R., and Greisen, E. W. (2002) 'Representations of Celestial Coordinates in FITS'. Astronomy and Astrophysics Vol. 395 pp. 1077–1122. https://doi.org/10.1051/0004-6361:20021327.

Chau J. L., McKay D., Vierinen J. P., La Hoz C., Ulich T., Lehtinen M., and Latteck R. (2018). Multi-static spatial and angular studies of polar mesospheric summer echoes combining MAARSY and KAIRA, Atmos. Chem. Phys., 18, 9547–9560, https://doi.org/10.5194/acp-18-9547-2018.

Chhetri R., J. Morgan, R. D. Ekers, J.-P. Macquart, E. M. Sadler, M. Giroletti, J. R. Callingham, S. J. Tingay (2018). Interplanetary scintillation studies with the Murchison Widefield Array – II. Properties of sub-arcsecond compact sources at low radio frequencies, Monthly Notices of the Royal Astronomical Society, Volume 474, Issue 4, March 2018, Pages 4937–4955, https://doi.org/10.1093/mnras/stx2864.

de Gasperin F., J. Vink, J. P. McKean, A. Asgekar, I. Avruch, M. J. Bentum, R. Blaauw, A. Bonafede, J. W. Broderick, M. Brüggen, F. Breitling, W. N. Brouw, H. R. Butcher, B. Ciardi, V. Cuciti, M. de Vos, S. Duscha, J. Eislöffel, D. Engels, R. A. Fallows, T. M. O. Franzen, M. A. Garrett, A. W. Gunst, J. Hörandel, G. Heald, M. Hoeft, M. Iacobelli, L.

https://doi.org/10.5194/egusphere-2026-1741
Preprint. Discussion started: 1 June 2026

V. E. Koopmans, A. Krankowski, P. Maat, G. Mann, M. Mevius, G. Miley, R. Morganti, A. Nelles, M. J. Norden, A. R. Offringa, E. Orrú, H. Paas, V. N. Pandey, M. Pandey-Pommier, R. Pekal, R. Pizzo, W. Reich, A. Rowlinson, H. J. A. Rottgering, D. J. Schwarz, A. Shulevski, O. Smirnov, C. Sobey, M. Soida, M. Steinmetz, M. Tagger, M. C. Toribio, A. van Ardenne, A. J. van der Horst, M. P. van Haarlem, R. J. van Weeren, C. Vocks, O. Wucknitz, P. Zarka, P. Zucca (2020). Cassiopeia A, Cygnus A, Taurus A, and Virgo A at ultra-low radio frequencies, Astronomy & Astrophysics (A&A), 635, A150, https://doi.org/10.1051/0004-6361/201936844

Dowell J., G. B. Taylor, F. Schinzel, N. E. Kassim, K. Stovall (2017), The LWA1 Low Frequency Sky Survey, Monthly Notices of the Royal Astronomical Society, Volume 469, Issue 4, August 2017, Pages 4537–4550, https://doi.org/10.1093/mnras/stx1136.

Fallows R. A., Coles W. A., McKay-Bukowski D., Vierinen J., Virtanen I. I., Postila M., Ulich T., Enell C.-F., Kero A., Iinatti T., Lehtinen M., Orispää M., Raita T., Roininen L., Turunen E., Brentjens M., Ebbendorf N., Gerbers M., Grit T., Gruppen P., Meulman H., Norden M. J., de Reijer J-P., Schoenmakers A., and Stuurwold K. (2014). Broadband meter-wavelength observations of ionospheric scintillation, Journal of Geophysical Research: Space Physics, 119, 10,544-10,560, doi:10.1002/2014JA020406.

Flisek P. Forte B., Fallows R., Kotulak K., Krankowski A, Bisi M. M., Mevius M., Błaszkiewicz L., Fron A., Tiburzi C., Soida M., Grzesiak M., Smierciak B., Matyjasiak B., Pozoga M., Dabrowski B., Mann G., Vocks C., and Zucca P. (2023). Towards the possibility to combine LOFAR and GNSS measurements to sense ionospheric irregularities, Journal of Space Weather and Space Climate, Vol. 13, N. 27, https://doi.org/10.1051/swsc/2023021.

Forte B. (2008), Refractive scattering evidence from multifrequency scintillation spectra observed at auroral latitudes, Radio Sci., 43, RS2012, doi:10.1029/2007RS003715.

Forte B., Smith N. D., Mitchell C. N., Da Dalt F., Panicciari T., Chartier A. T., Stevanovic D., Vuckovic M., Kinrade J., Tong J. R., Häggström I., and Turunen E. (2013). Comparison of temporal fluctuations in the total electron content estimates from EISCAT and GPS along the same line of sight, Annales Geophysicae, Vol. 31, pp. 745–753, https://doi.org/10.5194/angeo-31-745-2013.

Forte B., Coleman C., Skone S., Häggström I., Mitchell C. N., Da Dalt F., Panicciari T., Kinrade J., and Bust G. (2017). Identification of scintillation signatures on GPS signals originating from plasma structures detected with EISCAT incoherent scatter radar along the same line of sight, Journal Geophysical Research: Space Physics, 122, pp. 916–931, DOI:10.1002/2016JA023271.

https://doi.org/10.5194/egusphere-2026-1741
Preprint. Discussion started: 1 June 2026

Forte B., Fallows R. A., Bisi M. M., Zhang J., Krankowski A., Dabrowski B., Rothkaehl H., and Vocks, C. (2022). Interpretation of Radio Wave Scintillation Observed through LOFAR Radio Telescopes. The Astrophysical Journal Supplement Series, Vol. 263(2), p.36, DOI 10.3847/1538-4365/ac6deb.

Forte B., Fallows R. A., Bisi M. M., Flisek P., Kotulak K., Krankowski A., Mevius M., and Beser K. (2023a), Use of scintillation observations from radio telescopes for the modelling of plasma irregularities, 20th Annual Meeting of the Asia Oceania Geosciences Society (AOGS), Singapore, 30/07/23 - 4/08/23.

Forte B., Fallows R. A., Bisi M. M., Flisek P., Kotulak K., Krankowski A., Mevius M., Beser K., Kero A, and Häggström I. (2023b). Observations of radio wave scintillation in the auroral ionosphere from various instruments, 20th Annual Meeting of the Asia Oceania Geosciences Society (AOGS), Singapore, 30/07/23 - 4/08/23.

Forte B., Fallows R. A., Bisi M. M., Flisek P. and Kotulak K. (2023c), 'Measurement of radio wave scintillation through radio telescopes', XXXVth URSI General Assembly and Scientific Symposium, Sapporo, Japan, 19/08/23 - 26/08/23.

Forte B., John H. M., Astin I., Arnold A., Allbrook T., Häggström I., and Vani B. C. (2023d). Propagation disturbances in the auroral and polar ionospheres investigated through EISCAT/ESR and their effects on positioning, XXXVth URSI General Assembly and Scientific Symposium, Sapporo, Japan, 19/08/23 - 26/08/23.

Forte B., Allbrook T., Arnold A., Astin I., Vani B. C., Francisco Galera Monico J., Shimabukuro M. H., Koulouri A., and John H. M. (2024). Methodology for the characterisation of the impact of TEC fluctuations and scintillation on ground positioning quality over South America and North Europe, with implications for forecasts, Advances in Space Research. https://doi.org/10.1016/j.asr.2024.02.033.

Fremouw E.J., Leadabrand R.L., Livingston R.C., Cousins M.D., Rino C.L., Fair B.C., and Long R.A. (1978). Early results from the DNA Wideband satellite experiment—Complex-signal scintillation. Radio Science, 13(1), pp.167-187, https://doi.org/10.1029/RS013i001p00167.

Gorgolewski S. (1965). The Advantages of a Lunar Radio Astronomy Observatory. Astronautica Acta, New Series, 11(2):130–131.

Hewish A., P. F. Scott and D. Wills (1964). Interplanetary scintillation of small diameter radio sources, Nature, Vol. 203, pp. 1214-1217, https://doi.org/10.1038/2031214a0.

https://doi.org/10.5194/egusphere-2026-1741
Preprint. Discussion started: 1 June 2026

Ishimaru A. (1978). Wave Propagation and Scattering in Random Media, Academic Press Inc. Re-issued by IEEE Press and Oxford University Press 1977.

Jakowski N., Sardon E., Engler E., Jungstand A., and Klähn D. (1996). Relationships between GPS-signal propagation errors and EISCAT observations, Ann. Geophys., 14, 1429–1436, https://doi.org/10.1007/s00585-996-1429-0.

John H. M., Forte B., Astin I., Allbrook T., Arnold A., Vani B. C., Häggström I., and Sato H. (2021a). An EISCAT UHF/ ESR experiment that explains how ionospheric irregularities induce GPS phase fluctuations at auroral and polar latitudes, Radio Science, 56, pp. 1-16, https://doi. org/10.1029/2020RS007236.

John H. M., Forte B., Astin I., Allbrook T., Arnold A., Vani B.C., and Häggström I. (2021b). Performance of GPS Positioning in the Presence of Irregularities in the Auroral and Polar Ionospheres during EISCAT UHF/ESR Measurements, Remote Sensing, 13(23), 4798, https://doi.org/10.3390/rs13234798.

Johnston G., Riddell A., and Hausler G. (2017). The International GNSS Service. Teunissen P. J. G., and Montenbruck O. (Eds.), Springer Handbook of Global Navigation Satellite Systems (1st ed., pp. 967-982), Cham, Switzerland: Springer International Publishing. DOI: 10.1007/978-3-319-42928-1.

Kelley M. C. (2009). The Earth's ionosphere: plasma physics and electrodynamics, Second Edition, Academic Press, San Diego, London.

Kero A., Vierinen J., McKay-Bukowski D., Enell C.-F., Sinor M., Roininen L., and Ogawa Y. (2014). Ionospheric electron density profiles inverted from a spectral riometer measurement, Geophysical Research Letters, Vol. 41, pp. 5370–5375, doi:10.1002/2014GL060986.

Kotulak K., Zakharenkova I., Krankowski A., Cherniak I., Wang N. and Fron A., (2020). Climatology characteristics of ionospheric irregularities described with GNSS ROTI, Remote Sensing, 12(16), 2634, pp. 1-20, doi:10.3390/rs12162634.

Kotulak K., Krankowski A., Fron A., Flisek P., Wang N., Li Z., Błaszkiewicz L. (2021). Sub-Auroral and Mid-Latitude GNSS ROTI Performance During Solar Cycle 24 Geomagnetic Disturbed Periods: Towards Storm's Early Sensing, Sensors, 21, 4325, pp. 1-18, https://doi.org/10.3390/s21134325.

https://doi.org/10.5194/egusphere-2026-1741
Preprint. Discussion started: 1 June 2026

Leick A., L. Rapoport, and D. Tatarnikov (2015). GPS Satellite Surveying, Fourth Edition, John Wiley & Sons, Inc., doi:10.1002/9781119018612.

Little L. T. and Hewish A. (1966). Interplanetary scintillation and its relation to the angular structure of radio sources, Monthly Notices of the Royal Astronomical Society, Volume 134, Issue 3, December 1966, Pages 221-237, https://doi.org/10.1093/mnras/134.3.221.

Loi, S. T., T. Murphy, I. H. Cairns, F. W. Menk, C. L. Waters, P. J. Erickson, C. M. Trott, N. Hurley-Walker, J. Morgan, E. Lenc, A. R. Offringa, M. E. Bell, R. D. Ekers, B. M. Gaensler, C. J. Lonsdale, L. Feng, P. J. Hancock, D. L. Kaplan, G. Bernardi, J. D. Bowman, F. Briggs, R. J. Cappallo, A. A. Deshpande, L. J. Greenhill, B. J. Hazelton, M. Johnston-Hollitt, S. R. McWhirter, D. A. Mitchell, M. F. Morales, E. Morgan, D. Oberoi, S. M. Ord, T. Prabu, N. Udaya Shankar, K. S. Srivani, R. Subrahmanyan, S. J. Tingay, R. B. Wayth, R. L. Webster, A. Williams, and C. L. Williams (2015), Real-time imaging of density ducts between the plasmasphere and ionosphere, Geophysical Research Letters, 42, 3707–3714, doi:10.1002/2015GL063699.

McKay D., Fallows R., Norden M., Aikio A., Vierinen J., Honary F., Marple S., and Ulich T. (2015). All-sky interferometric riometry, Radio Science, 50, 1050–1061, October 2015, doi:10.1002/2015RS005709.

McKay-Bukowski D., Vierinen J., Virtanen I. I., Fallows R., Postila M., Ulich T, Wucknitz O., Brentjens M., Ebbendorf N., Enell C.-F., Gerbers M., Grit T., Gruppen P., Kero A., Iinatti T., Lehtinen M., Meulman H., Norden M.,
Orispää M., Raita T., de Reijer J. P., Roininen L., Schoenmakers A., Stuurwold K., and Turunen E. (2015). KAIRA: The Kilpisjärvi Atmospheric Imaging Receiver Array — System Overview and First Results, in IEEE Transactions on Geoscience and Remote Sensing, Vol. 53, N. 3, pp. 1440–1451, doi: 10.1109/TGRS.2014.2342252.

McKay D. (2018) KAIRA – Kilpisjärvi Atmospheric Imaging Receiver Array; Design, Operations and First Scientific Results, PhD Thesis, University of Tromsø, http://hdl.handle.net/10037/13716.

Morgan J. S., J.-P. Macquart, R. Ekers, R. Chhetri, M. Tokumaru, P. K. Manoharan, S. Tremblay, M. M. Bisi, and B. V. Jackson (2018). Interplanetary Scintillation with the Murchison Widefield Array I: a sub-arcsecond survey over 900 deg^2 at 79 and 158 MHz, Monthly Notices of the Royal Astronomical Society, MNRAS 473, pp. 2965–2983, doi:10.1093/mnras/stx2284.

Morgan J. S. , Macquart J.-P., Chhetri R., Ekers R. D., Tingay S. J. and Sadler E. M. (2019). Interplanetary Scintillation with the Murchison Widefield Array V: An all-sky survey of compact sources using a modern low-frequency radio telescope.

https://doi.org/10.5194/egusphere-2026-1741
Preprint. Discussion started: 1 June 2026

Publications of the Astronomical Society of Australia 36, e002, 1–17. https://doi.org/10.1017/pasa.2018.40.

Morgan, J., McCauley P. I., Waszewski A., Ekers R., and Chhetri R. (2023). Detection and characterization of a Coronal Mass Ejection using Interplanetary Scintillation measurements from the Murchison Widefield Array. Space Weather, 21, e2022SW003396, https://doi.org/10.1029/2022SW003396.

Narayan, R. (1992). The physics of pulsar scintillation. Philosophical Transactions of the Royal Society of London. Series A: Physical and Engineering Sciences, 341(1660), pp.151-165, DOI: 10.1098/rsta.1992.0090.

Papitashvili N. E. and King J. H. (2020), OMNI Hourly Data" [magnetic field, proton density, solar wind plasma speed], NASA Space Physics Data Facility, https://doi.org/10.48322/1shr-ht18, accessed on 11 February 2025.

Pi X., Mannucci A. J., Lindqwister U. J., and Ho C. M. (1997). Monitoring of global ionospheric irregularities using the worldwide GPS network, Geophysical Research Letters, 24(18), pp. 2283-2286, https://doi.org/10.1029/97GL02273.

Pohjolainen S., McKay D., Talebpour Sheshvan N., and Monstein C. (2023). Repeated Type III Burst Groups Associated with a B-Class Flare and a Narrow-Width CME, Solar Physics, Vol. 298, N. 118, https://doi.org/10.1007/s11207-023-02212-8.

The Astropy Collaboration, A. M. Price-Whelan, B. M. Sipőcz, H. M. Günther, P. L. Lim, S. M. Crawford, S. Conseil, D. L. Shupe, M. W. Craig, N. Dencheva, A. Ginsburg, J. T. VanderPlas, L. D. Bradley, D. Pérez-Suárez, M. de Val-Borro, (Primary Paper Contributors), T. L. Aldcroft, K. L. Cruz, T. P. Robitaille, E. J. Tollerud, (Astropy Coordination Committee), C. Ardelean, T. Babej, Y. P. Bach, M. Bachetti, A. V. Bakanov, S. P. Bamford, G. Barentsen, P. Barmby, A. Baumbach, K. L. Berry, F. Biscani, M. Boquien, K. A. Bostroem, L. G. Bouma, G. B. Brammer, E. M. Bray, H. Breytenbach, H. Buddelmeijer, D. J. Burke, G. Calderone, J. L. Cano Rodríguez, M. Cara, J. V. M. Cardoso, S. Cheedella, Y. Copin, L. Corrales, D. Crichton, D. D'Avella, C. Deil, É. Depagne, J. P. Dietrich, A. Donath, M. Droettboom, N. Earl, T. Erben, S. Fabbro, L. A. Ferreira, T. Finethy, R. T. Fox, L. H. Garrison, S. L. J. Gibbons, D. A. Goldstein, R. Gommers, J. P. Greco, P. Greenfield, A. M. Groener, F. Grollier, A. Hagen, P. Hirst, D. Homeier, A. J. Horton, G. Hosseinzadeh, L. Hu, J. S. Hunkeler, Ž. Ivezić, A. Jain, T. Jenness, G. Kanarek, S. Kendrew, N. S. Kern, W. E. Kerzendorf, A. Khvalko, J. King, D. Kirkby, A. M. Kulkarni, A. Kumar, A. Lee, D. Lenz, S. P. Littlefair, Z. Ma, D. M. Macleod, M. Mastropietro, C. McCully, S. Montagnac, B. M. Morris, M. Mueller, S. J. Mumford, D. Muna, N. A. Murphy, S. Nelson, G. H. Nguyen, J. P. Ninan, M. Nöthe, S. Ogaz, S. Oh, J. K. Parejko, N. Parley, S. Pascual, R. Patil, A. A. Patil, A. L. Plunkett, J. X. Prochaska, T. Rastogi, V. Reddy Janga, J. Sabater, P. Sakurikar, M. Seifert, L. E. Sherbert, H. Sherwood-Taylor, A. Y. Shih, J. Sick, M. T. Silbiger, S. Singanamalla, L. P. Singer, P. H. Sladen, K. A. Sooley, S. Sornarajah, O. Streicher, P. Teuben, S. W. Thomas, G. R. Tremblay, J. E. H. Turner, V. Terrón, M. H. van Kerkwijk, A. de la Vega, L. L. Watkins, B. A. Weaver, J. B. Whitmore, J. Woillez, V. Zabalza, and (Astropy Contributors)

https://doi.org/10.5194/egusphere-2026-1741
Preprint. Discussion started: 1 June 2026

(2018), The Astropy Project: Building an Open-science Project and Status of the v2.0 Core Package, The Astronomical Journal, Volume 156, Number 3, https://doi.org/10.3847/1538-3881/aabc4f.

Takeaki K. and H. Kurata (2004). Generalized Least Squares, John Wiley & Sons, Ltd., doi:10.1002/0470866993.

Tong Y. L. (2012). The Multivariate Normal Distribution, Springer-Verlag New York Inc., https://doi.org/10.1007/978-1-4613-9655-0.

van Haarlem M. P., Wise M. W., Gunst A. W., Heald G., McKean J. P., Hessels J. W. T., de Bruyn A. G., Nijboer R., Swinbank J., Fallows R., Brentjens M., Nelles A., Beck R., Falcke H., Fender R., Hörandel J., Koopmans L. V. E., Mann G., Miley G., Röttgering H., Stappers B. W., Wijers R. A. M. J., Zaroubi S., van den Akker M., Alexov A., Anderson J., Anderson K., van Ardenne A., Arts M., Asgekar A., Avruch I. M., Batejat F., Bähren L., Bell M. E., Bell M. R., van Bemmel I., Bennema P., Bentum M. J., Bernardi G., Best P., Bîrzan L., Bonafede A., Boonstra A.-J., Braun R., Bregman J., Breitling F., van de Brink R. H., Broderick J., Broekema P. C., Brouw W. N., Brüggen M., Butcher H. R., van Cappellen W., Ciardi B., Coenen T., Conway J., Coolen A., Corstanje A., Damstra S., Davies O., Deller A. T., Dettmar R.-J., van Diepen G., Dijkstra K., Donker P., Doorduin A., Dromer J., Drost M., van Duin A., Eislöffel J., van Enst J., Ferrari C., Frieswijk W., Gankema H., Garrett M. A., de Gasperin F., Gerbers M., de Geus E., Grießmeier J.-M., Grit T., Gruppen P., Hamaker J. P., Hassall T., Hoeft M., Holties H. A., Horneffer A., van der Horst A., van Houwelingen A., Huijgen A., Iacobelli M., Intema H., Jackson N., Jelic V., de Jong A., Juette E., Kant D., Karastergiou A., Koers A., Kollen H., Kondratiev V. I., Kooistra E., Koopman Y., Koster A., Kuniyoshi M., Kramer M., Kuper G., Lambropoulos P., Law C., van Leeuwen J., Lemaitre J., Loose M., Maat P., Macario G., Markoff S., Masters J., McFadden R. A., McKay-Bukowski D., Meijering H., Meulman H., Mevius M., Middelberg E., Millenaar, Miller-Jones R. J. C. A., Mohan R. N., Mol J. D., Morawietz J., Morganti R., Mulcahy D. D., Mulder E., Munk H., Nieuwenhuis L., van Nieuwpoort R., Noordam J. E., Norden M., Noutsos A., Offringa A. R., Olofsson H., Omar A., Orrú E., Overeem R., Paas H., Pandey-Pommier M., Pandey V. N., Pizzo R., Polatidis A., Rafferty D., Rawlings S., Reich W., de Reijer J.-P., Reitsma J., Renting G. A., Riemers P., Rol E., Romein J. W., Roosjen J., Ruiter M., Scaife A., van der Schaaf K., Scheers B., Schellart P., Schoenmakers A., Schoonderbeek G., Serylak M., Shulevski A., Sluman J., Smirnov O., Sobey C., Spreeuw H., Steinmetz M., Sterks C. G. M., Stiepel H.-J., Stuurwold K., Tagger M., Tang Y., Tasse C., Thomas I., Thoudam S., Toribio M. C., van der Tol B., Usov O., van Veelen M., van der Veen A.-J., ter Veen S., Verbiest J. P. W., Vermeulen R., Vermaas N., Vocks C., Vogt C., de Vos M., van der Wal E., van Weeren R., Weggemans H., Weltevrede P., White S., Wijnholds S. J., Wilhelmsson T., Wucknitz O., Yatawatta S., Zarka P., Zensus A., and van Zwieten J. (2013). LOFAR: The LOw-Frequency ARray, Astronomy and Astrophysics, Vol. 556, N. A2, DOI: 10.1051/0004-6361/201220873.

https://doi.org/10.5194/egusphere-2026-1741
Preprint. Discussion started: 1 June 2026

Virtanen I. I., McKay-Bukowski D., Vierinen J., Aikio A., Fallows R., and Roininen L. (2014), Plasma parameter estimation from multistatic, multibeam incoherent scatter data, J. Geophys. Res. Space Physics, Vol. 119, pp. 10,528–10,543, doi:10.1002/2014JA020540.

Wanninger L. (1993). The occurrence of ionospheric disturbances above Japan and their effects on precise GPS positioning, in 8th International Symposium on Recent Crust Movements (CRCM 93), Kobe, Japan.

Uscinski B. J. (1977), The elements of wave propagation in random media, McGraw-Hill.

van Cittert P. H. (1934), Die Wahrscheinliche Schwingungsverteilung in Einer von Einer Lichtquelle Direkt Oder Mittels Einer Linse Beleuchteten Ebene, Physica, Vol. 1, Issues 1–6, pp. 201-210, https://doi.org/10.1016/S0031-8914(34)90026-4.

Waszewski A, Morgan J., and Jordan C. H. (2022). A measurement of small-scale features using ionospheric scintillation. Comparison with refractive shift measurements. Publications of the Astronomical Society of Australia 39, e036, 1–11, https://doi.org/10.1017/pasa.2022.33.

Yamauchi Y., Tokumaru M., Kojima M., Misawa M., Mori H., Takaba H., Kondo T., Tanaka T., Manoharan P.K. and Esser R. (1996). Observations of micro-turbulence in the solar wind near the sun with interplanetary scintillation. In AIP Conference Proceedings (Vol. 382, No. 1, pp. 366-366), American Institute of Physics, doi: 10.1063/1.51472.

Zernike F. (1938), The concept of degree of coherence and its application to optical problems, Physica, Vol. 5, Issue 8, pp. 785-795, https://doi.org/10.1016/S0031-8914(38)80203-2.